Early View publication on wileyonlinelibrary.com
(issue and page numbers not yet assigned;
citable using Digital Object Identifier – DOI)

Laser Photonics Rev., 1–33 (2011) / **DOI** 10.1002/lpor.201100020

LASER & PHOTONICS
REVIEWS

Abstract Silicon photonics leverages the optical, electrical and material properties of silicon and the mature complementary metal-oxide semiconductor (CMOS) nanofabrication technique to develop on-chip photonic integration, which has been making significant impacts in various frontiers including next-generation optical communications networks, on-chip optical interconnects for high-speed energy-efficient computing and biosensing. Among many optical structures fabricated on silicon chips, microresonators due to their high-Q resonances and small footprints play important roles in various devices including lasers, filters, modulators, switches, routers, delays, detectors and sensors. This paper reviews from a microresonator perspective some of the latest progress in the field, summarizes design considerations in various applications and points out key challenges and potentials.

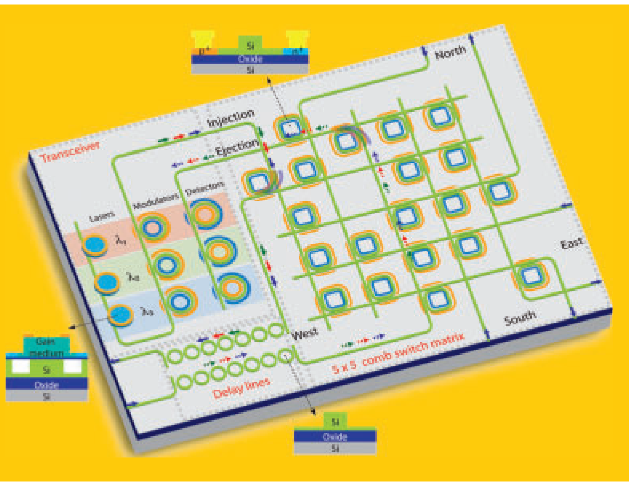

Silicon photonics: from a microresonator perspective

Shaoqi Feng[1], **Ting Lei**[1], **Hui Chen**[1,2], **Hong Cai**[1], **Xianshu Luo**[1,3], **and Andrew W. Poon**[1,*]

1. Introduction

Optical microresonators [1–7] that partially confine light by total internal reflection (TIR) at the dielectric microresonator sidewalls are versatile microphotonic structures featuring compact size, wavelength selectivity and resonance field enhancement. Although the idea of TIR-based microresonators can be dated back to the 1960s [8], only over the past two decades research of microresonator-based devices as key building blocks for integrated photonic applications has come of age [9], thanks to the advance of micro/nanofabrication technologies and a wide scope of technological demands spanning optical communications, on-chip optical interconnects and biosensing. Various material systems have been proposed and demonstrated as possible substrates for microresonators including silicon [9], silica [10], compound III-V semiconductors [11], polymers [12] and compound glass [13].

Silicon, which is a well-understood material for microelectronics, offers useful properties for integrated photonic applications. The silicon transparency in the fiber-optic telecommunications wavelengths (1.3–1.6 μm) enables light transmission in waveguides fabricated on silicon-on-insulator (SOI) substrates. The silicon waveguide core of refractive index ~ 3.45 interfaced with silica cladding of refractive index ~ 1.44 provides a large refractive-index contrast for tight optical confinement in a compact device footprint. The state-of-the-art SOI submicrometer-sized waveguide propagation loss in the 1550-nm wavelength range is in the order of 1 dB/cm [14], which is considered sufficient for on-chip optical interconnects applications. Leveraging complementary metal-oxide-semiconductor (CMOS) fabrication technology, silicon photonics thus promises large-scale integration and potentially low-cost mass production in a CMOS foundry. Besides the SOI platform, deposited thin films such as silicon nitride (SiN), silicon oxynitride (SiON), polysilicon, germanium (Ge), silicon-germanium (SiGe) also enable a myriad of CMOS-compatible silicon photonic technologies.

This review is about recent developments in silicon photonics from a microresonator perspective. Every device reviewed in the article is based on silicon microresonator technology. The work reviewed in the article covers almost all the devices demonstrated in silicon photonics, including filters, modulators, switches, routers, delays, detectors and sensors. Primarily driven by our own work and experience in photonic devices, we chose to focus our review on some recent developments in silicon microresonator technologies for applications in optical communications, on-chip optical interconnects and optofluidic biosensing. We reluctantly skip many on-going exciting developments such as hybrid silicon and Ge-on-silicon lasers [15], nonlinear optics in silicon waveguides [16], materials for silicon photonics [17–19], integration [20–23], optomechanics [24], and silicon photonic crystals (PC) based devices [25], which we believe have been amply reviewed in recent articles and book chapters [26–29]. In this regard, this article is by no means an exhaustive review of silicon photonics but it

---

[1] Photonic Device Laboratory, Department of Electronic and Computer Engineering, The Hong Kong University of Science and Technology, Clear Water Bay, Hong Kong SAR, China [2] Current address: State Key Laboratory of Optoelectronic Materials and Technologies, School of Physics and Engineering, Sun Yat-Sen University, Guangzhou 510275, China [3] Current address: Institute of Microelectronics, A*STAR (Agency of Science, Technology and Research), 11 Science Park Road, Singapore Science Park II, Singapore 117685
[*] Corresponding author: e-mail: eeawpoon@ust.hk

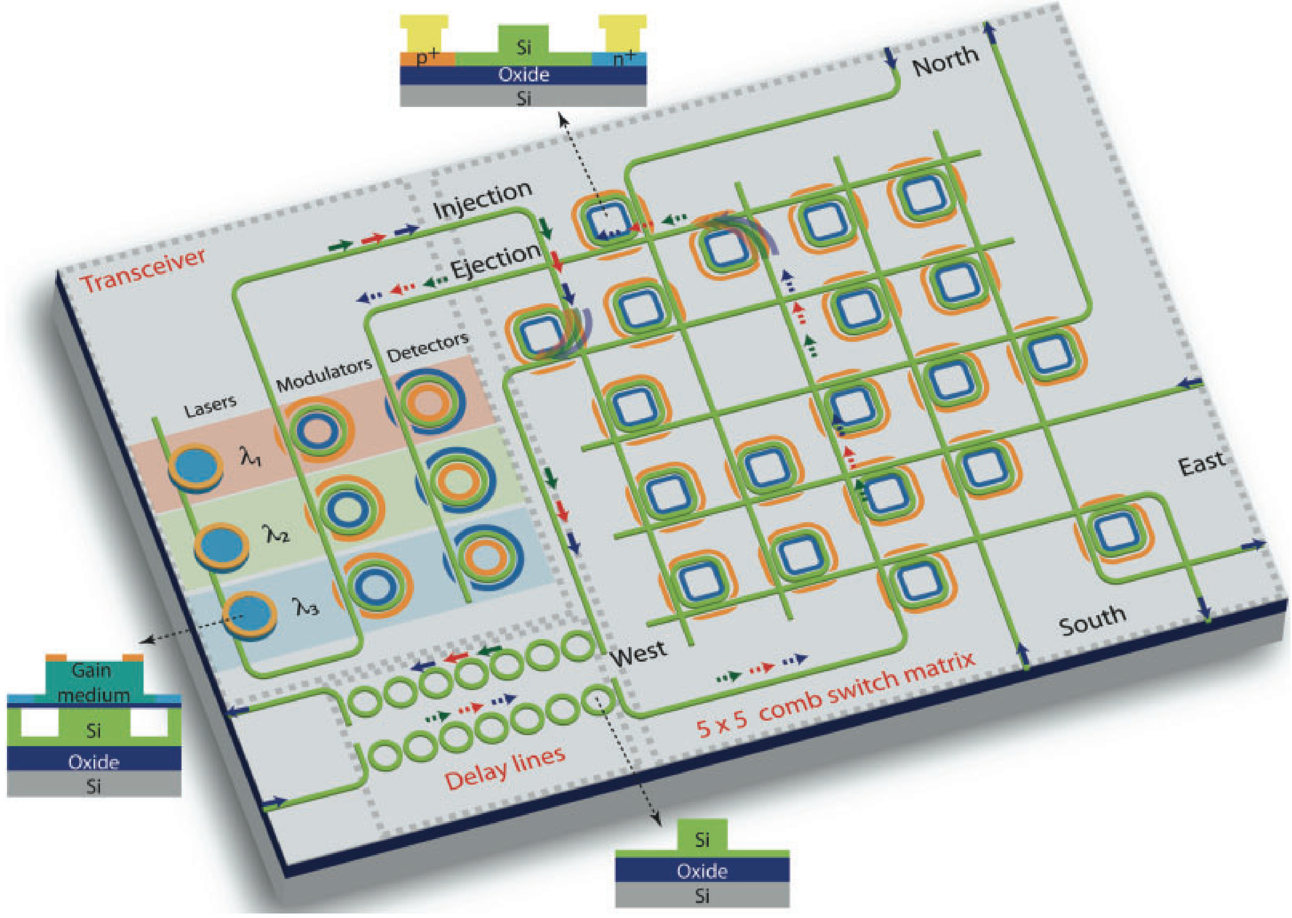

Figure 1 (online color at: www.lpr-journal.org) Artist's impression of a silicon photonic chip for on-chip optical interconnects on a SOI substrate. The photonic chip comprises a transceiver connected to a 5-input-port-to-5-output-port (North, East, South, West, Injection and Ejection) multiwavelength comb switch matrix with broadband optical delay lines for incoming and outgoing signals in one of the ports. The transceiver comprises on-chip hybrid silicon microlasers, wavelength-selective modulators and photodetectors designed for the wavelength channels λ_1, λ_2 and λ_3. All the functional components utilize microresonator-based passive and active devices. The solid (dashed) arrows illustrate three modulated λ channels injected (ejected) by the transceiver are routed by the switch matrix toward (incoming from) the West port. Insets show the cross-sectional schematics of the hybrid silicon microdisk lasers, p-i-n diodes integrated in microring resonators for modulators, switches and detectors, and passive SOI coupled-microring resonator optical waveguides for broadband optical delay lines.

merely represents how the authors look at the current state-of-the-art and possible future developments from our own microresonator perspective.

Figure 1 shows an artist's impression of a silicon photonic chip comprising microresonator-based passive and active devices for on-chip optical interconnects on a SOI substrate. The photonic chip comprises a transceiver connected to a 5-input-port-to-5-output-port (North, East, South, West, Injection and Ejection) multiwavelength comb switch matrix with broadband optical delay lines for incoming and outgoing signals in one of the ports. The transceiver comprises on-chip hybrid silicon microlasers emitting at three different wavelength channels λ_1, λ_2 and λ_3, wavelength-selective electro-optical (EO) modulators and photodetectors designed for each of the wavelength channels. Such optical interconnects could potentially enable multiple computing cores to be communicating on multiple wavelength channels with flexible data rates / formats, reconfigurable routes and delays, with potentially low power consumption [30–32].

Figure 2 shows our concept of an optofluidic chip with microfluidic channels / chamber integrated with microresonator-based devices on a SiN-on-silica substrate. The photonic layer routes visible or near-infrared light. The microresonator-based devices enable on-chip optical manipulation of micro/nanoparticles (transporting, dropping, buffering, sensing and sorting) and label-free biosensing of analyte and nanoparticles in fluids. Such optofluidic chips could potentially enable low-cost and disposable lab-on-a-chip applications [33, 34].

In this paper we discuss the principles, designs and modeling, fabrication and characterization of such silicon-based microresonator devices, and review their state-of-the-art, issues and mitigations. The rest of the paper is divided into the

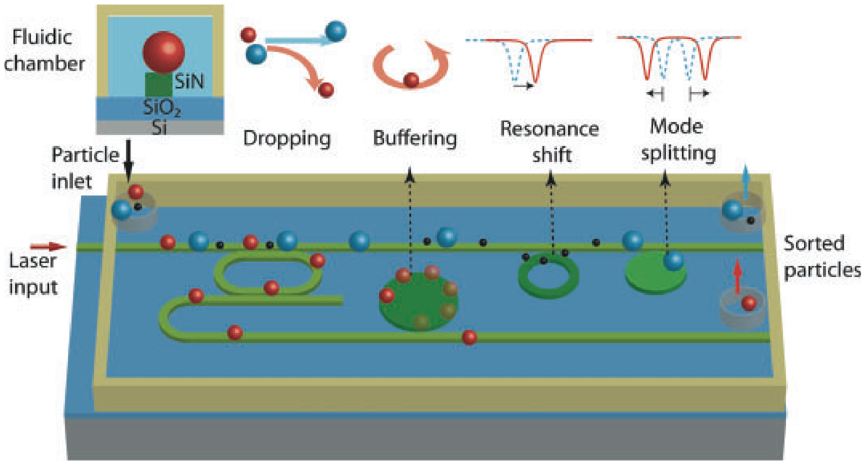

Figure 2 (online color at: www.lpr-journal.org) Artist's impression of a silicon optofluidic chip on a silicon nitride (SiN)-on-silica substrate. The optofluidic chip comprises an optical microresonator-based on-chip micro- and nanoparticle manipulation circuit integrated with optical biosensors. The particle circuit enables the functionalities of particles transport / dropping / buffering / sorting. The biosensors detect the biomaterial concentrations or binding events by means of resonance wavelength shifts and mode splitting. The microfluidic chamber serves to confine the fluidic and the particle flow.

following sections: Sect. 2 on fundamentals of waveguide-coupled microresonators, Sect. 3 on silicon microresonator loss mechanisms, Sect. 4 on waveguide coupling to silicon microresonators, Sect. 5 on novel-shaped microresonators, Sect. 6 on optical filters design, modeling and performance, Sect. 7 on optical modulators, Sect. 8 on optical switches and routers, Sect. 9 on coherent control of resonance lineshapes, Sect. 10 on optical delay lines, Sect. 11 on sub-bandgap wavelength-selective p-i-n photodetectors, Sect. 12 on optical signal processing, Sect. 13 on optical biosensing and Sect. 14 on microparticle manipulation in optofluidic chips. We will summarize the review with future challenges and an outlook in Sect. 15.

2. Fundamentals of waveguide-coupled microresonators

Here we begin with a brief discourse on basic concepts of waveguide-coupled optical microresonators. Figure 3a schematically shows a microresonator side-coupled with a bus waveguide. Light is launched from the waveguide input port and evanescently coupled into and out of the microresonator in the coupling region through submicrometer-sized gap spacing. The light in the microresonator is partially confined along the cavity sidewall by TIR.

The cavity field phase-matches with the input-coupled field upon each round trip, giving rise to an optical resonance. The resonance phase-matching condition is as follows:

$$n_{\text{eff}} L = m\lambda_m, \tag{1}$$

where n_{eff} is the effective refractive index of the microresonator, L is the cavity round-trip length ($\approx 2\pi R$ with R the circular microresonator radius), λ_m is the mth-order resonance wavelength, and m is the integer number of wavelengths along an optical round-trip length (termed azimuthal mode number).

The free-spectral range (FSR) is given as:

$$\text{FSR} = \frac{\lambda_m^2}{n_g L}, \tag{2}$$

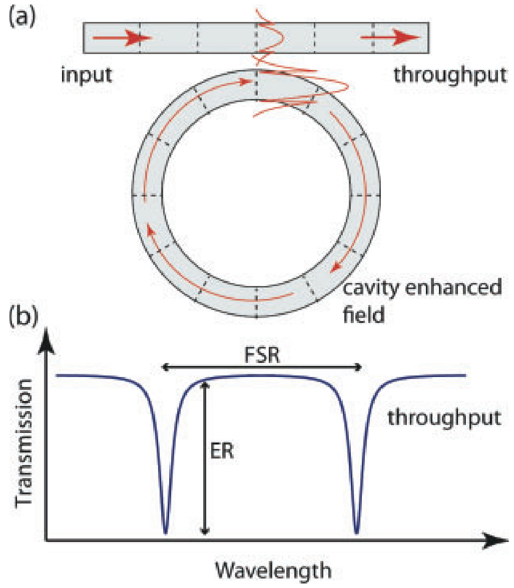

Figure 3 (online color at: www.lpr-journal.org) (a) Schematic of a waveguide-coupled microring resonator. Arrows indicate the traveling-wave propagation directions. Dashed lines show the wavefronts matching between the microring and the bus waveguide. Schematic field profiles illustrate the cavity field enhancement of the microresonator relative to the bus waveguide. (b) Schematic of the throughput transmission spectrum showing the single-mode microring resonances. FSR: free-spectral range. ER: extinction ratio.

where n_g is the group index, which is defined as:

$$n_{\text{g}} = n_{\text{eff}} - \lambda \frac{\text{d}n_{\text{eff}}}{\text{d}\lambda}, \tag{3}$$

where λ is the free-space wavelength. Figure 3b schematically shows the throughput transmission spectrum of a waveguide-coupled microring resonator exhibiting resonances spaced by one FSR. The resonance exhibits an inverted Lorentzian lineshape that is proportional to:

$$\frac{-(\delta\lambda/2)^2}{(\lambda-\lambda_m)^2 + (\delta\lambda/2)^2}, \tag{4}$$

where $\delta\lambda$ is the resonance linewidth. The resonance extinction ratio (ER) is defined as the ratio of intensity at on-resonance wavelength to that at off-resonance wavelength. Such resonance spectral response thus enables wavelength selectivity, which is fundamental in various microresonator-based passive devices such as optical filters, modulators, switches, routers, detectors, and active devices such as on-chip lasers.

The quality (Q) factor is used to characterize the loss of energy in a microresonator, which is defined as

$$Q = 2\pi \frac{\text{stored energy}}{\text{energy loss per round trip}}. \tag{5}$$

The Q factor for a resonance at wavelength λ_m can also be obtained from the transmission spectrum as

$$Q = \frac{\lambda_m}{\delta\lambda}. \tag{6}$$

In a waveguide-coupled microresonator, the energy loss per round-trip is due to intrinsic optical losses in the cavity, namely light scattering, radiation loss and absorption (see Sect. 3), and extrinsic output-coupling loss by the coupled waveguide. The total Q factor of a waveguide-coupled microresonator therefore comprises two contributions: the intrinsic quality factor Q_0 and the coupling quality factor Q_c. The Q_0 factor is related to the intrinsic cavity power loss coefficient α. The Q_c factor is related to the field-coupling coefficient κ. The relations of Q, Q_0, Q_c, α and κ are described as follows

$$Q^{-1} = Q_0^{-1} + Q_c^{-1} \tag{7}$$

$$Q_0 = \omega_0 \tau_0 = \frac{2\pi n_g}{\alpha \lambda_0} \tag{8}$$

$$Q_c = \omega_0 \tau_c = \frac{\omega_0}{|\kappa|^2 / \tau_{rt}}, \tag{9}$$

where τ_0 is the intrinsic cavity energy 1/e lifetime, τ_c is the extrinsic waveguide-coupling energy 1/e lifetime, τ_{rt} is the round-trip light propagation time, ω_0 is the cavity resonance angular frequency and λ_0 is the cavity resonance free-space wavelength. Therefore, based on Eqs. (7)–(9), the Q factor in principle can be varied by properly designing or tuning α, κ, n_g, and τ_{rt}.

The optical power transmittance $T(\omega)$ of a waveguide-coupled microresonator around a certain resonance frequency ω_0 depends on the coupling regime [35, 36] given as

$$T(\omega) = \left| \frac{1/Q_0 - 1/Q_c + i(\omega - \omega_0)/\omega_0}{1/Q_0 + 1/Q_c + i(\omega - \omega_0)/\omega_0} \right|^2. \tag{10}$$

The coupling regime depends on the balance between the waveguide coupling and the intrinsic cavity loss. There are three coupling regimes, namely (i) undercoupling ($Q_c > Q_0$), (ii) critical coupling ($Q_c = Q_0$) and (iii) overcoupling ($Q_c < Q_0$). Figure 4 shows the modeled power transmittance using Eq. (10) at a resonance frequency ω_0 and the modeled Q/Q_0 using Eq. (7) in the three coupling regimes. In the critical-coupling regime, the throughput optical power transmission at resonance ω_0 is null in principle. The modeled Q drops monotonically from the undercoupling regime to the overcoupling regime.

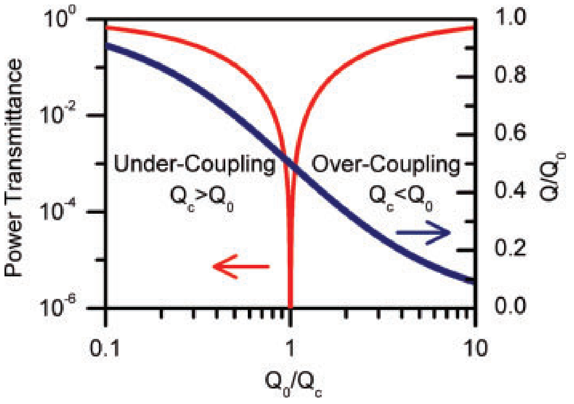

Figure 4 (online color at: www.lpr-journal.org) Modeled throughput power transmittance (red curve, left axis) and resonance Q/Q_0 (blue curve, right axis) as a function of Q_0/Q_c in a waveguide-coupled microresonator. Q: total quality factor, Q_0: intrinsic quality factor, Q_c: coupling quality factor.

The microresonators exhibit strong phase response around the resonance, which can be used for engineering the transmission dispersion and time delay.

Figure 5 shows the modeled transmission intensity, phase response and corresponding time delay in under- and overcoupling regimes. The modeling is based on the standard transfer matrix method [35]. Here, we assume a 20-μm radius microring resonator with Q of 10^4 and ER of 20 dB. In the undercoupling regime ($Q_c > Q_0$), there is an anomalous phase response at the resonance wavelength, which

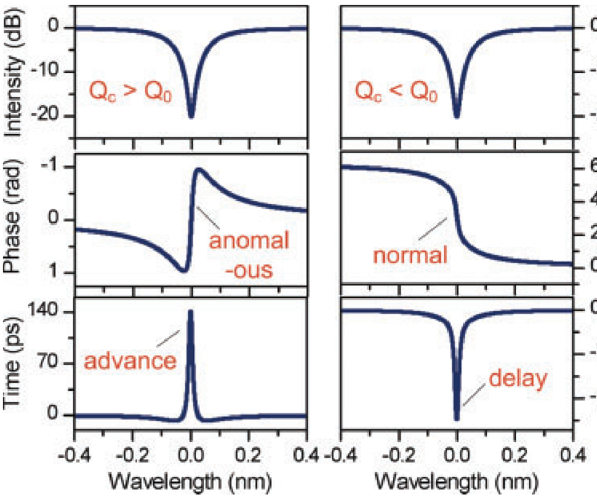

Figure 5 (online color at: www.lpr-journal.org) Modeled resonance throughput transmission intensity, phase response and time delay / advance of a waveguide-coupled microring resonator in the undercoupling regime (left column) and the overcoupling regime (right column).

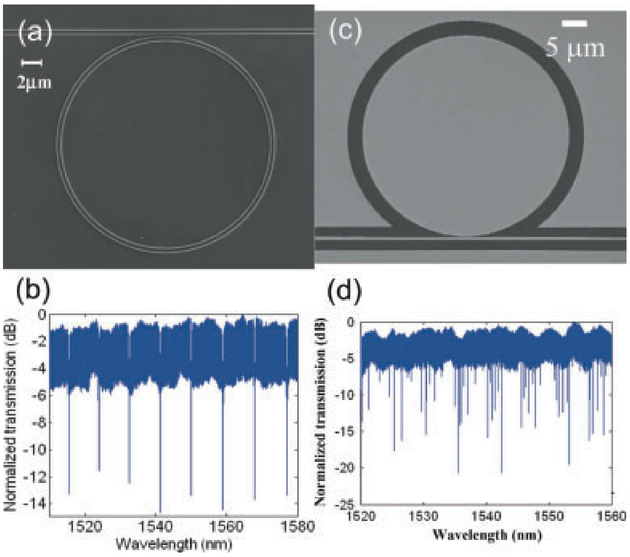

Figure 6 (online color at: www.lpr-journal.org) (a) SEM of a silicon waveguide-coupled 10-μm radius microring resonator. (b) Measured transmission spectrum of the microring resonator showing single-mode resonances. (c) SEM of a silicon waveguide-coupled 20-μm radius microdisk resonator. (d) Measured transmission spectrum of the microdisk resonator showing multiple whispering-gallery modes. Reproduced with permission from [36], ©2010 IEEE.

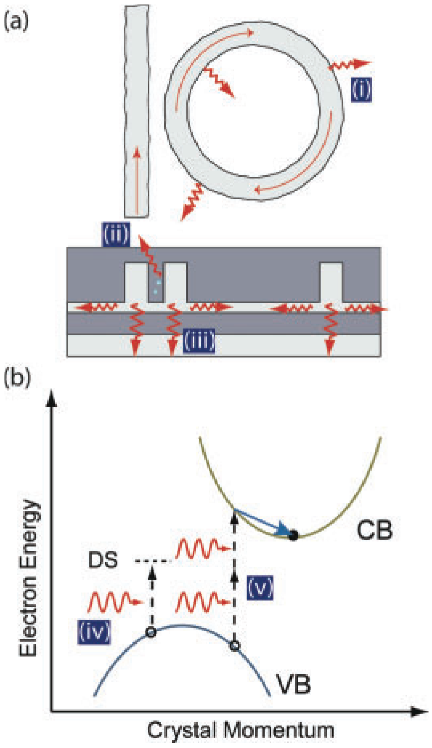

Figure 7 (online color at: www.lpr-journal.org) Schematics of optical loss mechanisms in silicon waveguide-coupled microresonators. (a) Radiation losses. (i) Surface-roughness-induced light scattering in the microresonator sidewalls. (ii) Optical leakage in the coupling gap between the side-coupled waveguide and the microresonator. (iii) Optical leakage from the undercladding layer to the silicon substrate and through the device slab layer. (b) Material absorption losses. (iv) Silicon surface-state absorption at surfaces or interfaces. (v) Silicon two-photon absorption. CB: conduction band. VB: valence band. DS: Defect state. Red arrows represent photons. Blue arrow represents phonon.

corresponds to time advance. In the overcoupling regime ($Q_c < Q_0$), there is a normal phase response at the resonance wavelength, which corresponds to time delay.

Silicon-based microresonators are often in the form of microring or microdisk resonators. A microring resonator is a ring-shaped waveguide structure that typically supports single-mode resonances. While a microdisk resonator is typically a circular disk structure that supports in general multiple-radial-order whispering-gallery modes (WGMs) that graze along the microdisk rim. Given a certain refractive-index contrast and cavity size, microring resonators that have both inner and outer sidewalls tend to suffer higher sidewall roughness-induced scattering loss (see Sect. 3, Fig. 7a), and thus in general exhibit a lower Q_0 factor than microdisk resonators that only have outer sidewalls.

Figure 6 shows, as examples, the scanning electron micrographs (SEMs) (Figs. 6a and c) and measured transmission spectra of a silicon waveguide-coupled 10-μm radius microring resonator (Fig. 6b) and a silicon waveguide-coupled 20-μm radius microdisk resonator (Fig. 6d) [36]. The microring resonator shows single-mode resonances with Q of $\sim 10^4$, while the microdisk resonator displays multiple WGMs with a Q of $\sim 10^6$.

3. Silicon microresonator loss mechanisms

Here, we discuss five dominant optical losses in silicon waveguide-coupled microresonators and briefly review mitigation methods. Figure 7a illustrates three of the mechanisms concerning scattering and radiation losses that are mainly related to the device structures and fabrication, namely (i) surface-roughness-induced scattering loss, (ii) scattering loss in the coupling gap spacing and (iii) optical leakage from the undercladding layer and the device slab layer. Figure 7b illustrates two of the mechanisms concerning subbandgap silicon absorption losses, namely (iv) linear surface-state absorption (SSA) at silicon surfaces or interfaces and (v) nonlinear two-photon absorption (TPA) in silicon bulk.

(i) Surface-roughness-induced scattering loss
Surface-roughness-induced scattering loss from the microresonator or waveguide sidewalls is largely due to the dry-etching process. In the case of a microring resonator with both inner and outer sidewalls, the scattering loss can be particularly severe compared with a microdisk resonator with only the outer sidewall. In order to mitigate the sidewall surface roughness, fabrication of silicon microresonator-based devices typically employs the forming and removal of an oxidation layer [37]. The oxidation process of silicon is usually

homogeneous, resulting in tens of nanometers of oxide that upon removal can effectively mitigate the surface roughness formed after the dry etching.

(ii) Scattering loss in the coupling gap spacing
The bus waveguide and the microresonator sidewalls in the coupling region inevitably scatter light. Besides, when the submicrometer-sized coupling gap spacing is not fully filled by the silica cladding layer, light is strongly scattered by the air voids. The latter can be mitigated by filling the gap spacing instead with boron phosphorus silicon glass followed by thermal reflow to eliminate air voids [38, 39].

(iii) Optical leakage from the undercladding layer and the device slab layer
Due to the submicrometer dimensions of silicon waveguides, the optical mode is largely exposed outside the waveguide core and significantly overlaps with the undercladding layer. In the case of silicon rib waveguides with a thin slab layer, optical leakage also occurs via the device layer. In order to reduce such optical leakage, the undercladding silica layer can be undercut by wet etching in buffered hydrofluoric acid. Such undercut microdisk resonators have been demonstrated with a Q value as high as 5×10^6 [40].

(iv) Linear subbandgap surface-state absorption at silicon surfaces or interfaces
Linear subbandgap absorption due to surface states on the silicon microresonator sidewalls can be more problematic than that due to those on the waveguide surfaces. This is because the cavity-enhanced field is expected to enhance the amount of field surface-state absorption per unit distance given a certain optical power. The absorption generates free carriers at the silicon microresonator sidewalls and thus is likely to result in free-carrier absorption (FCA). Besides, the absorbed power also generates heat. The details of the SSA mechanism and its effects, however, vary with the detailed surface morphologies and device interfaces and are therefore difficult to be quantitatively modeled or controlled [41–43]. One mitigation method on silicon microresonators is to passivate the silicon surfaces with SiN, which reduces the density of the surface dangling bonds.

(v) Nonlinear subbandgap two-photon absorption in silicon bulk
TPA is a nonlinear subbandgap absorption that increases quadratically with the silicon waveguide power and cavity-stored energy for wavelengths shorter than 2.2 µm. As the TPA-generated free carriers are primarily inside the bulk of the silicon microresonator, the free carriers are likely to have a relatively long recombination lifetime compared with those generated from the SSA at the silicon microresonator sidewalls. Moreover, these TPA-induced free carriers in the silicon microresonator bulk have a significant spatial overlap with the optical mode field, and in turn give rise to more significant FCA. The FCA rate thus increases in a quadratic manner relative to the coupled power. Miniaturizing the microresonator size in general escalates the TPA and FCA rates as the higher power density in a smaller mode volume promotes these nonlinear optic effects.

Whereas the TPA-induced FCA can be readily mitigated as the generated free carriers can be efficiently swept out by integrating a p-i-n diode into the microresonator and reverse-biasing the diode [44–46], TPA remains unavoidable. It is thus necessary to take this nonlinear absorption into account when using silicon microresonators for handling relatively high optical powers, especially in potential multiwavelength systems for on-chip optical interconnects where the comb switch (see Fig. 1) may carry a large amount of optical power from multiple wavelength channels.

4. Waveguide coupling to silicon microresonators

The coupling coefficient κ defined in Eq. (9) can be calculated by using coupled-mode theory and first-order perturbation approximation as follows [36, 47]

$$\kappa = -\frac{\mathrm{i}\omega_0\varepsilon_0\sqrt{\tau_{\mathrm{rt}}}}{4}\int_{-\infty}^{+\infty}\iint_A dz dA\Delta(n^2)\frac{E_{\mathrm{r}}^*}{\sqrt{U}}\frac{E_{\mathrm{w}}}{\sqrt{P}}\mathrm{e}^{\mathrm{i}m\varphi-\mathrm{i}\beta z}, \tag{11}$$

where E_r^* is the conjugate of the microresonator mode field, E_w is the waveguide mode field, U is the microresonator mode energy, P is the waveguide mode power, φ is the microresonator mode azimuthal angular phase, β is the waveguide propagation constant, z is the field position in the waveguide propagation direction, $\Delta(n^2)$ is the relative permittivity perturbation due to the coupled waveguide and A is the waveguide cross-sectional area. Thus, κ depends on the phase mismatch of $(m\varphi - \beta z)$ between the microresonator mode and the waveguide mode, and also the spatial overlap between the two mode profiles.

Efficient waveguide-coupling imposes phase matching between the waveguide and the microresonator. In the case of a small-sized microring resonator, however, the phase mismatch between the straight single-mode bus waveguide and the tightly curved microring waveguide of the same dimension becomes significant as the microring radius shrinks to the range of few micrometers. It is thus of the essence to carefully design different widths for the straight bus waveguide and the microring resonator a few micrometers in size, in order to enable proper phase matching between the bus waveguide and the microring [36, 48].

The mode-profile overlap is related to the submicrometer-sized coupling gap spacing between the bus waveguide and the microresonator. For submicrometer-sized waveguide structures with high refractive-index contrast, such coupling gap spacing is typically of the order of 100–300 nm, and thus the fabrication requires advanced lithography technologies such as electron-beam (e-beam) lithography or deep-UV (DUV) photolithography. However, fabrication of such critical features with high fidelity and uniformity even across a chip is technologically challenging.

Waveguide coupling to a high index contrast silicon-based microresonator is also typically constrained by the short interaction length between the circular microring/disk resonator and the straight waveguide. In order to enhance the interaction length, the conventional approach is to employ a racetrack microring resonator comprising two 180°-curved waveguide sections seamlessly joined to two straight waveguide sections for directional coupling to bus waveguides along a long interaction length. This relaxes the tight constraint on the coupling gap spacing. However, the modal mismatch between the straight waveguide section and the curved waveguide section introduces additional radiation loss, which often compromises the Q factor. Silicon racetrack microring resonators are therefore typically used only for applications that do not demand high Q factors.

Another common approach to enable efficient waveguide-to-microring resonator coupling is to use multimode-interference (MMI) coupler design [49]. The MMI coupler design also offers the advantages of less wavelength-dependent coupling and less sensitivity to fabrication errors. Nonetheless, a major drawback of such MMI couplers is additional insertion loss at the transitions between the single-mode waveguide and the MMI region.

Compared with microring resonators, waveguide coupling to a circular microdisk resonator is often less efficient. This is in part due to the fact that the waveguide mode is often not exactly phase matched with the microdisk WGMs. The waveguide mode also only spatially overlaps with the lower-order WGMs that propagate closer to the microdisk rim. In order to enhance the waveguide-coupling efficiency of a microdisk resonator, one conventional approach is to lengthen the waveguide interaction length by using a curved waveguide wrapped along a portion of the microdisk circumference. Another common method is by tailoring the device slab layer thickness [36], which, however, also tends to increase the device optical leakage (see Sect. 3).

5. Novel-shaped microresonators

In order to address the waveguide-to-microresonator coupling issue, especially to ease the submicrometer-sized coupling gap spacing constraint for silicon-based microdisk resonators, our research group over the years has put significant effort into designing noncircular-shaped microdisk resonators. We proposed and demonstrated two different approaches using novel-shaped microdisk resonators [50], namely (1) polygonal microdisk resonators with a long flat sidewall for directional evanescent coupling via a relatively wide coupling gap spacing, and (2) microspiral and double-notch-shaped microdisk resonators with a single or two notches for gapless nonevanescent coupling.

5.1. Polygonal microdisk resonators

Figs. 8a and b show the finite-difference time-domain (FDTD) simulated continuous-wave field patterns of the waveguide coupling to a flat-sidewall microdisk and to a curved-sidewall microdisk [50]. When the waveguide is coupled to a flat-sidewall microdisk, the coupled wave shows flat wavefronts with a directional wavevector. The wavevector direction depends on the coupled waveguide width. By properly designing the single-mode waveguide width, we can match the wavevector of the waveguide-coupled wave

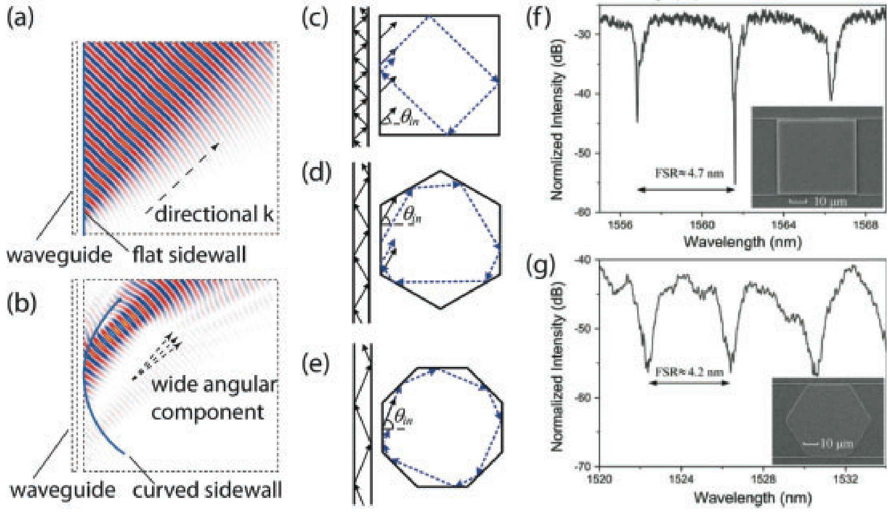

Figure 8 (online color at: www.lpr-journal.org) (a) and (b) FDTD-simulated continuous-wave field patterns of waveguide coupling to (a) a flat sidewall showing directional propagating wavefronts and (b) a curved sidewall showing converging then diverging wavefronts. (c)–(e) Ray-picture schematics of the light coupling between the bus waveguide and the polygonal microdisk resonators and the N-bounce modes inside the microdisks for (c) square-, (d) hexagonal- and (e) octagonal-shaped microresonators. θ_{in}: ray incident angle along the input-coupling sidewall. (f) Measured TE-polarized throughput transmission spectrum of a 50-μm sized square-shaped microdisk resonator on a SOI substrate. Inset: Top-view SEM of the square-shaped microdisk resonator. (g) Measured TE-polarized throughput transmission spectrum of a 50-μm sized round-cornered hexagonal-shaped microdisk resonator on a SOI substrate . Inset: Top-view SEM of the hexagonal-shaped microdisk resonator. Reproduced with permission from [51], ©2006 IEEE.

with that of the microdisk resonance modes. When the waveguide is coupled to a curved-sidewall microdisk, the coupled wave shows curved wavefronts that indicates an angular spread in the wavevector. Therefore, it is difficult to selectively couple the waveguide mode to a particular WGM in the conventional circular microdisk.

Figure 8c shows a round-trip ray trajectory in a square microdisk resonator [50]. The lightwave with a propagation direction of around 45° to the sidewall is totally internally reflected and forms a 4-bounce round-trip orbit. The 4-bounce mode can be decomposed into two orthogonal Fabry–Perot normal modes between opposite sidewalls of the square microdisk resonator. As such, square microdisk resonators support standing-wave resonances [51]. The concept can be generalized to polygonal microdisk resonators with sidewall number N (e.g. $N = 6, 8$).

Figures 8d and e show N bounce modes for hexagonal and octagonal microdisk resonators. The N bounce modes with their specific wavevector angles can be phase matched with the side-coupled waveguide of a particular width and cross-sectional design, as suggested in Fig. 8a.

Figure 8f shows the measured throughput transmission spectrum of a waveguide-coupled square microdisk resonator with side length of 50 µm in a SOI substrate [51]. The coupling gap spacing is about 0.35 µm. The spectrum displays single modes with a Q of 4000 and an ER of 27 dB. The FSR of 4.7 nm is consistent with a 4-bounce mode. The inset shows the SEM of the waveguide-coupled square microdisk.

Figure 8g shows the measured throughput transmission spectrum of a waveguide-coupled hexagonal microdisk resonator with side length of 50 µm in a SiN substrate [51]. The coupling gap spacing is again about 0.35 µm. The spectrum exhibits a Q of 1500 and an ER of 15 dB. The FSR of 4.2 nm is consistent with a 6-bounce mode. The inset shows the SEM of the waveguide-coupled hexagonal microdisk.

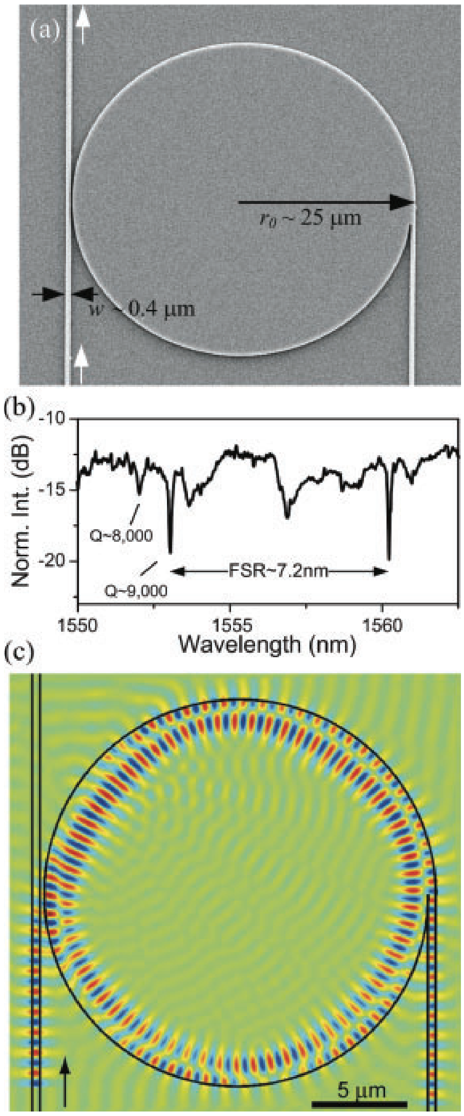

Figure 9 (online color at: www.lpr-journal.org) (a) SEM of the fabricated spiral-shaped microdisk resonator with 25 µm radius and 0.4-µm notch width on a SiN substrate. Reproduced with permission from [53], ©2007 OSA. (b) Measured TM-polarized transmission spectrum of the fabricated device. Reproduced with permission from [53], ©2007 OSA. (c) FDTD-simulated mode field pattern of a spiral-shaped microdisk resonator with 10 µm radius and 0.4 µm notch width on a SiN substrate. Reproduced with permission from [54], ©2009 OSA.

5.2. Gapless-coupled microdisk resonators

Spiral-shaped microdisk resonators applied to silicon photonics have been inspired by the pioneering work of unidirectional lasing from an InGaN spiral-shaped micropillar demonstrated by Chern et al [52].

Figure 9a shows the SEM of the waveguide-coupled spiral-shaped microdisk resonator on a SiN substrate [53]. The device comprises a spiral-shaped microdisk resonator, a single-mode waveguide that is seamlessly butt-coupled to the spiral notch, and another single-mode waveguide that is evanescently side coupled to the cavity. The spiral shape is defined as

$$r(\varphi) = r_0(1 - \varepsilon\varphi/2\pi), \tag{12}$$

where r_0 is the spiral radius at azimuthal angle $\varphi = 0$ and ε is the shape parameter. The notch enables gapless coupling from a bus waveguide, where the waveguide mode field spatially overlaps with the whispering-gallery-like resonator mode field.

Figure 9b shows the measured transmission spectrum at the side-coupled bus waveguide exhibiting resonances with a highest Q value of ~ 9000 and an ER exceeding 5 dB [53].

Figure 9c shows the FDTD-simulated resonance mode field pattern of a spiral-shaped SiN microdisk resonator with a radius of 10 µm and a notch of 0.4 µm. The spiral-shaped microdisk modes are, however, quite sophisticated and different from the WGMs in a circular-shaped microdisk due to the breakdown of the rotational symmetry.

The double-notch-shaped microdisk resonator is another nonuniform-shaped microdisk resonator that enables gapless coupling.

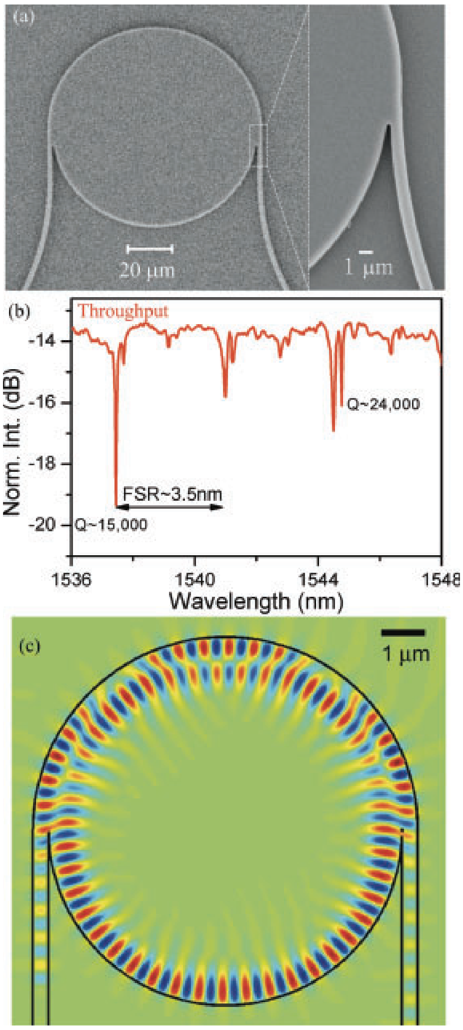

Figure 10 (online color at: www.lpr-journal.org) (a) SEM of the fabricated double-notch-shaped microdisk resonator with 25 µm radius and 1 µm notch width on a SiN substrate. Inset: zoom-in of the notch-coupled waveguide. Reproduced with permission from [54], ©2007 OSA. (b) Measured transmission spectrum of the device. Reproduced with permission from [54], ©2007 OSA. (c) FDTD-simulated mode field pattern of a double-notch-shaped microdisk resonator with 4.25 µm radius and 0.32 µm notch width on a SiN substrate. Reproduced with permission from [54], ©2009 OSA.

Figure 10a shows the SEM of a fabricated double-notch-shaped microdisk resonator on a SiN substrate [54]. The shape comprises two seamlessly joined semicircles of slightly different radii and preserves mirror symmetry with respect to the center axis. The inset shows the zoom-in view of the gapless coupling region, where the waveguide mode field spatially overlaps and couples to the resonator mode.

Figure 10b shows the measured transmission spectrum at the butt-coupled bus waveguide exhibiting resonances with Q factors in the range of 15 000 to 24 000 [54].

Figure 10c shows the FDTD-simulated resonance mode field pattern of a double-notch-shaped microdisk resonator with a radius of 4.25 µm and a notch of 0.32 µm.

However, in both cases of spiral-shaped and double-notch-shaped microdisk resonators, the details of the gapless coupling mechanism regarding the phase mismatch and the mode spatial overlap between the notch-coupled waveguide mode and the microdisk modes still require further study.

The waveguide coupling to novel-shaped microresonators can be designed in order to attain desirable coupling strength. For polygonal microdisk resonators, we can design the gap width and the interaction length in the evanescent coupling region. For gapless-coupled microdisk resonators, we can design the notch width and the notch angle in the gapless coupling region. However, the novel-shaped microresonators discussed here are still sensitive to the fabrication imperfection as traditional microrings and microdisks are, for instance, the resonance wavelengths are sensitive to the physical dimension of the microresonators.

6. Optical filters design, modeling and performance

One early proposed application of silicon-based microresonator technology is optical wavelength channel filtering for wavelength-division multiplexing (WDM) telecommunications applications, in which the wavelength channel adding and dropping functionalities are required. As such, optical add-drop filters comprising input and output waveguides coupled with microresonators have been widely investigated. Optical add-drop filters for WDM high-data-rate telecommunications applications require demanding performances on the filter responses, namely, a wide FSR of tens of nm for single-channel filtering in the telecommunication C-band (1530–1565 nm) and a box-like transmission profile with a sufficiently wide bandwidth of tens of GHz for 10–40 Gbit/s data transmission.

The wide FSR imposes a relatively small-sized silicon microring resonator with a radius smaller than 5 µm. The small cavity size, however, limits the Q_0 factor, and thus requires specific coupling and loss designs. The bus-waveguide width should be narrower than the microring waveguide width in order to phase match the straight-waveguide mode with the curved-waveguide mode. Following such coupling design, the microring resonator with the smallest radius of 1.5 µm has been demonstrated [48]. In order to minimize the waveguide propagation loss, both the waveguide and microring waveguide widths can be relatively wide ($\sim$ 600 nm) [55]. Besides, the wide FSR can also be attained by Vernier filter design [56] that employs two relatively large-sized microresonators of slightly different sizes.

The optical filter should also have a flat-top response and a fast roll-off in order to reject adjacent channels by > 30 dB. Single microresonators that exhibit a Lorentzian resonance lineshape, however, cannot satisfy such stringent performance requirements. One possible approach to tailor the filter response is high-order coupled-microresonator-based filters.

Figure 11 illustrates the analytically modeled drop-port transmission spectra of a single microring resonator-based

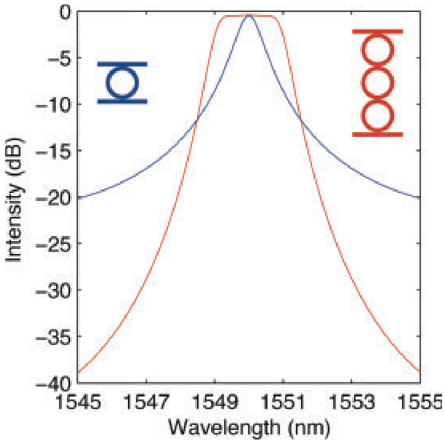

Figure 11 (online color at: www.lpr-journal.org) Modeled drop-port transmission spectra (normalized to the input) of a single microring resonator-based add-drop filter (blue) and a third-order cascaded microring resonator-based add-drop filter (red). The blue spectrum shows a Lorentzian lineshape resulting from a single resonance. The red spectrum shows a box-like lineshape resulting from mode splitting of three intercavity coupled identical resonators. Insets: schematic structures of the filters.

channel add-drop filter that exhibits a Lorentzian lineshape and a third-order cascaded microring resonator-based channel add-drop filter that exhibits a flat-top, box-like lineshape. For high-order coupled-microring resonator-based filters, the waveguide-to-microring field coupling coefficient κ_{WR} and the microring-to-microring field coupling coefficient κ_{RR} are typically different. Here, we choose $\kappa_{WR} = 0.3$ and $\kappa_{RR} = 0.7$ in order to attain the flat-top, box-like lineshape, assuming three identical 10-µm radius microrings.

Third-order coupled-microring resonator-based filters have been demonstrated. Table 1 summarizes the state-of-the-art of the silicon-based third-order coupled-microring resonator-based filters.

Figure 12a shows the SEM of such a fabricated filter on a SiN substrate [57]. The waveguide widths for the mi-

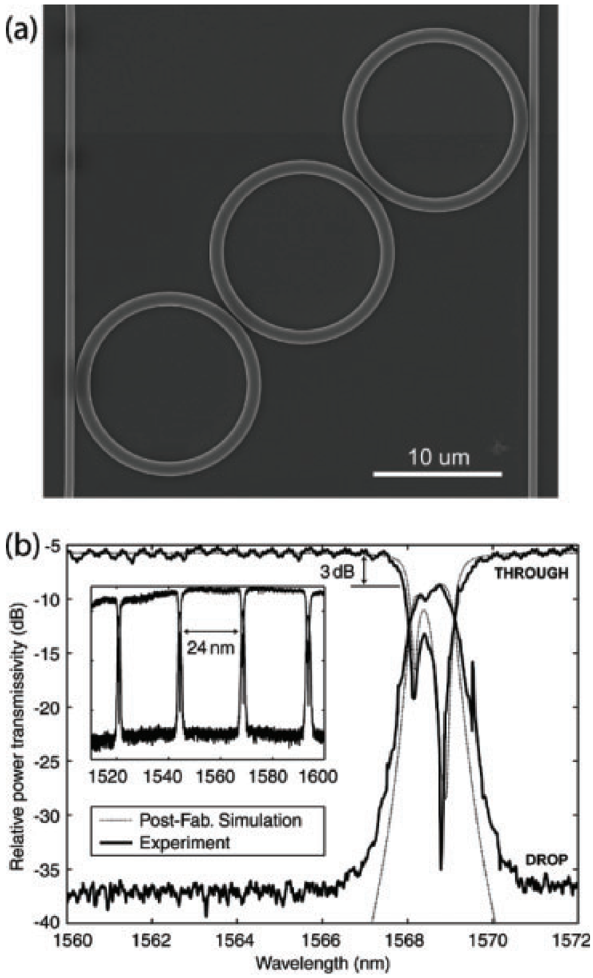

Figure 12 (online color at: www.lpr-journal.org) (a) SEM of a third-order cascaded coupled-microring resonator-based add-drop filter on a SiN substrate. (b) Measured and simulated transmission spectra of the fabricated device showing box-like drop-port transmission. Inset: measured filter response over multiple FSRs. Reproduced with permission from [57], ©2004 OSA.

Table 1 Key design parameters and measured performances of silicon-based high-order coupled-microresonator-based filters.

	[57]	[58]	[59, 60]	[61]
Platform	SiN	Si	Si	Si
Resonator element	Ring	Ring	Racetrack	Racetrack
Ring/bus-waveguide width (nm)	1050/850	600/500	500/500	500/500
Ring-to-ring/ring-to-bus-waveguide coupling gap spacings (nm)	268/80	350/100	120/– (MMI couplers)	120/45
Ring-to-bus-waveguide coupling length (µm)	–	–	3.5	7
Bend radius (µm)	7.3	2.5	4	3
Footprint (µm^2)	∼ 1000	75	70	40
FSR (nm)	24	32	18	18
Drop-port loss (dB)	3	–	< 3	< 0.3
1-dB bandwidth (GHz)	88	125	310	∼ 100
In-band throughput-port extinction (dB)	7	20	–	12
Out-of-band drop rejection (dB)	30	40	30	18
Roll-off (dB/GHz)	∼ 0.2	∼ 0.2	∼ 0.2	∼ 0.8

croring resonator and the bus waveguide were designed to be slightly different in order to satisfy the phase-matching condition. The coupling gap spacing were also tailored in order to attain the required coupling coefficients.

Figure 12b shows the measured transmission spectrum that exhibited a wide and flat-top pass-band of 88 GHz, fast roll-off of 0.2 dB/GHz and high out-of-band rejection ratio of 30 dB [57]. However, due to the relatively low index contrast of SiN waveguides, the microring radius of 7.3 μm was relatively large in order to enable good optical confinement.

Compared with the SiN platform, the SOI substrate offers higher index contrast and thus enables photonic devices with more compact sizes. Ultracompact microring resonators with 2.5 μm radius have been demonstrated [58]. Interresonator coupling between microring resonators is, however, still difficult to control. One can better tailor the interresonator coupling by using racetrack microring resonators [59–61].

7. Optical modulators

Optical modulators are essential components for on-chip optical interconnects and telecommunications applications. The requirements for the modulators include modulation speed and depth, power consumption and drive voltage [62]. High-speed modulation above 10 Gbit/s data rate with low energy consumption of 10 fJ/bit are targeted. In terms of modulation depth, although a relatively large extinction of > 7 dB is always preferred for interconnect applications, a moderate modulation depth of 4–5 dB is believed to be sufficient. In order to be supported by CMOS driving circuits, the driving voltage swing V_{pp} should be around 1 V.

Research work on silicon optical modulators has been comprehensively reviewed in a recently published article [62]. Here, we therefore only highlight silicon microresonator-based EO modulators, which offer the key merits of compact size, wavelength selectivity and potentially low power consumption compared with the Mach–Zehnder interferometer (MZI)-based modulators. We also limit the scope of the discussion on the modulation mechanism to only the widely adopted free-carrier dispersion (FCD) effect. In silicon microresonator-based modulators, modulation based on carrier injection and depletion has been demonstrated. Table 2 summarizes the state-of-the-art of the silicon microresonator-based EO modulators.

The empirical equations [63] for FCD-induced refractive-index change Δn and absorption coefficient change $\Delta\alpha$ as functions of the change of free electrons and free holes concentrations at 1.55 μm are given as:

$$\begin{aligned}\Delta n &= \Delta n_{\mathrm{e}} + \Delta n_{\mathrm{h}} \\ &= -(8.8 \times 10^{-22} \Delta N_{\mathrm{e}} + 8.5 \times 10^{-18} \Delta N_{\mathrm{h}}^{0.8}) \qquad (13)\end{aligned}$$

$$\begin{aligned}\Delta\alpha &= \Delta\alpha_{\mathrm{e}} + \Delta\alpha_{\mathrm{h}} \\ &= 8.5 \times 10^{-18} \Delta N_{\mathrm{e}} + 6.0 \times 10^{-18} \Delta N_{\mathrm{h}}\,, \qquad (14)\end{aligned}$$

where Δn_{e} is the refractive-index change resulting from change in free-electron carrier concentrations ΔN_e (cm^{-3}), Δn_{h} is the refractive-index change resulting from change in free-hole carrier concentrations ΔN_h (cm^{-3}), $\Delta\alpha_{\mathrm{e}}$ is the absorption coefficient change resulting from ΔN_e, and $\Delta\alpha_{\mathrm{h}}$ is the absorption coefficient change resulting from ΔN_h.

7.1. Carrier-injection modulators

Figure 13a illustrates optical intensity modulation by blueshifting a resonance wavelength through carrier injection in a p-i-n diode embedded microresonator. For a fixed carrier wavelength positioned at the resonance upon zero

Table 2 Key measured performances of silicon microresonator-based optical modulators.

Structure		Diameter (μm)	Q	ER (dB)	Tuning efficiency (pm/V)	BW (GHz)	Speed (Gbit/s)	Energy (fJ/bit)	V_{pp} (V)	MD (dB)	IL (dB)	Ref.
I	Ring	12	39 350	15	30	–	1.5	–	6.9	6	1	[65]
I	Ring	12	12 000	–	–	–	18	–	4	3	–	[66]
I	Disk	10	16 900	7	70	0.5	0.5	–	6.9	7	1	[67]
D	Racetrack	24	10 000	23	42	–	12.5	10	1	8	4	[68]
D	Ring	15	8300	14	10	–	5	400	2	3	6	[69]
D	Racetrack	12	3000	20	–	19	–	–	–	–	–	[70]
D	Ring	30	14 500	15	18	11	10	50	2	6.5	2	[71]
D	Ring	60	8000	20	–	10	10	–	–	–	–	[72]
D	Racetrack	80	9000	–	2.3	8	12.5	–	4	1	10	[73]
D	Racetrack	96	9800	–	–	–	30	335	1.6	3.3	–	[74]
D	Disk	4	10 000	8	45	–	10	85	3.5	8	2	[75]
D	Disk	3	10 000	10	65	–	12.5	3	1	4	5	[76]

I: injection. D: depletion. ER: extinction ratio. BW: bandwidth. V_{pp}: voltage swing. MD: modulation depth. IL: insertion loss. Diameter of a racetrack resonator is defined as the racetrack circumference divided by π.

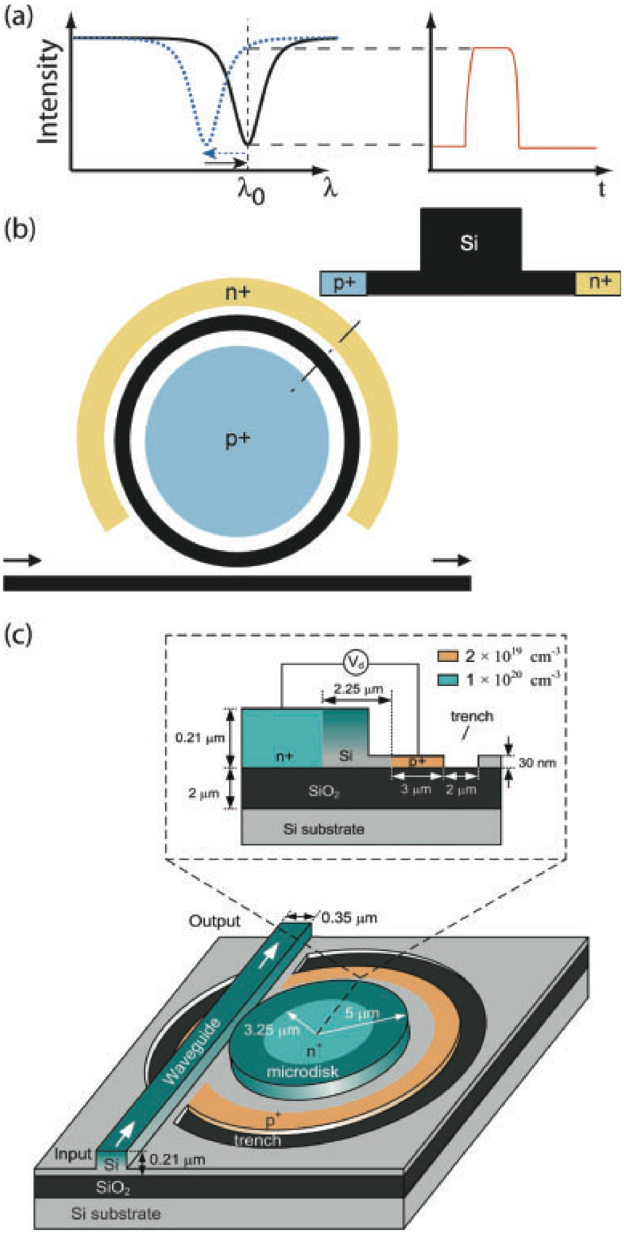

Figure 13 (online color at: www.lpr-journal.org) Optical intensity modulation using a silicon p-i-n diode embedded microresonator in carrier-injection mode. (a) The resonance wavelength blueshifts upon injecting free carriers. The intensity at a carrier wavelength is modulated as the resonance wavelength is shifted back and forth. λ_0: carrier wavelength. (b) Top-view schematic of the microring-resonator-based carrier-injection-mode modulator. Inset: Cross-sectional schematic of the p-i-n diode integrated waveguide. Reproduced with permission from [65], ©2005 NPG. (c) Schematic of the microdisk-resonator-based carrier-injection-mode modulator. Inset: cross-sectional view of the lateral p-i-n diode. Reproduced with permission from [67], ©2006 OSA.

carrier injection, the resonance blueshift driven by the electrical signal determines the modulation depth of the optical signal. Narrow resonance linewidth with steep spectral slope is desirable in order to attain sufficient modulation depth under a particular voltage swing. However, the cavity photon lifetime (typically $\sim$ 1–10 ps) should be significantly shorter than the data bit slot (e.g. $\sim$ 100 ps for 10 Gbit/s data rate) for the cavity field to build up and decay without distorting the signal. This sets the microresonator Q to be of the order of 10^3–10^4 for 10–40 Gbit/s modulation. For a microresonator with a Q factor of 5000, the resonance wavelength needs to be blueshifted by 0.2 nm in order to attain maximum intensity change. Such a blueshift requires injected carrier concentration change at the level of 10^{18} cm^{-3} according to Eq. (13).

The spectral tuning speed corresponding to the rise edge of the optical modulation is limited by the carrier diffusion time. The fall edge of the optical modulation is limited by the minority carrier lifetime, which can be minimized by sweeping out the minority carriers upon a reverse bias. The drive voltage for 12.5 Gbit/s modulation has been demonstrated to be as low as 3 V [64]. However, for on-chip applications, the drive voltage should be further reduced to about 1 V to be compatible with CMOS drive circuits.

Xu et al [65] pioneered carrier-injection microresonator-based silicon EO modulators in 2005, where they demonstrated a modulation speed of 1.5 Gbit/s.

Figure 13b shows a schematic of the microring resonator-based modulator integrated with a lateral p-i-n diode. The modulation speed for this early work was limited by the fact that only part of the microring was integrated with the p-i-n diode. In a follow-up work, they surrounded the entire microring with a p-i-n diode and improved the modulation speed to 18 Gbit/s using a pre-emphasis driving signal [66]. The short impulses at the rising and falling edges of the signal enabled fast injection and extraction.

Our group demonstrated the first carrier-injection-based p-i-n diode embedded silicon microdisk modulator in 2006 [67].

Figure 13c shows the cross-sectional and perspective schematics of the device [67]. We designed the intrinsic region of the p-i-n diode to be in the vicinity of the microdisk rim where the WGMs propagate, and the doped regions to be in the central portion of the microdisk (n^+) and outside the microdisk sidewall by 0.5 μm (p^+). As such we enabled selective spatial overlap between the WGM field and the injected carriers, while minimizing the scattering and absorption losses due to the heavily doped regions and the metal contacts. The subgigahertz modulation speed demonstrated was, however, mainly limited by the relatively wide p-i-n diode intrinsic region of 2.25 μm that lengthened the diffusion time and the nonoptimized metal contacts that resulted in a relatively large resistance–capacitance (RC) time.

7.2. Carrier-depletion modulators

Figure 14a illustrates optical intensity modulation by redshifting a resonance wavelength through carrier depletion in a p-n diode embedded microresonator. The modulation speed due to the carrier depletion (upon the carrier drift velocity) is significantly faster than the carrier injection (upon

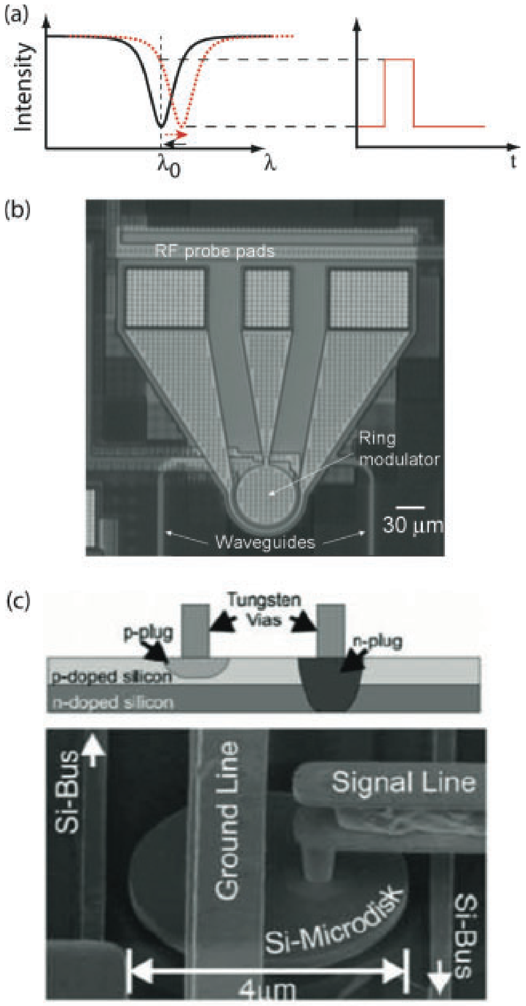

Figure 14 (online color at: www.lpr-journal.org) Optical intensity modulation using a silicon p-n diode embedded microresonator in carrier-depletion mode. (a) The resonance wavelength redshifts upon depleting free carriers. The intensity at a carrier wavelength is modulated as the resonance wavelength is shifted back and forth. λ_0: carrier wavelength. (b) Optical micrograph of the microring-resonator-based carrier-depletion-mode modulator. Reproduced with permission from [72], ©2006 IEEE. (c) Top-view SEM and cross-sectional schematic of the microdisk-resonator-based carrier-depletion-mode modulator. Reproduced with permission from [75], ©2008 IEEE.

the carrier diffusion velocity). While the depletion modulator can work beyond 10 Gbit/s, the injection modulator can reach 10 Gbit/s modulation speed with a pre-emphasis driving signal (see Table 2). The depletion-mode modulation speed is typically limited by the RC time constant of the p-n diode. However, the resonance wavelength tuning efficiency (resonance wavelength shift to drive voltage) is typically lower than that in the injection-mode modulator (see Table 2). The maximum carrier concentration change is determined by the doping concentration in the p-n junction. Given a moderate doping concentration of 10^{18} cm^{-3}, the depletion-induced resonance wavelength redshift assuming fully depleted depletion region is only ~ 0.1 nm, according to Eq. (13). Such resonance wavelength redshift is typically within the resonance linewidth, assuming a moderate resonance Q factor, thus rendering severe limitations on the modulation depth to few dB [68, 69].

In order to enhance the wavelength-tuning efficiency, the spatial overlap between the optical mode and the carrier density change in the depletion region needs to be optimized [70, 71]. The optical waveguide with a compact dimension can confine the optical mode in a relatively small volume that preferentially overlaps with the depletion region. The horizontal p-n junction can be asymmetrical both in the doped region width and in the doping concentrations in order to maximize the spatial overlap between the optical mode and the hole depletion, which could induce a larger index change compared with electron depletion according to Eq. (13).

Gunn [72] demonstrated the first carrier-depletion microresonator-based silicon EO modulator in 2006. Figure 14b shows the optical micrograph of the 30-µm radius microring modulator. The 3-dB modulation bandwidth was shown to be 10 GHz. The following work from various groups generally improved the modulator performance towards higher speed and lower power consumption [70, 71, 73]. For compatibility with CMOS technology, the driving voltage swing was reduced to 1 V [68]. The modulator with integrated electrical driving circuit made by a 90-nm CMOS fabrication process has also been demonstrated [69]. Most recently, the modulation speed has been pushed to 30 Gbit/s [74].

The carrier-depletion-type silicon microdisk modulator was demonstrated in 2008 [75]. Figure 14c shows the SEM of the 4-µm diameter microdisk modulator, which was embedded with a vertical p-n junction. The metal contacts were kept within the interior of the microdisk. The microdisk outer sidewall enabled a significant spatial overlap between the WGMs and the depletion region. The structure was further improved by the same group in 2010 [76]. In their later work, a 3.5-µm diameter silicon microdisk resonator was embedded with the p-n diode along only π radians of the microdisk. Both the junction resistance and capacitance were reduced, thus enabling high-speed operation. The resonance Q factor was improved to enable a steeper roll-off by reducing the dopant-induced loss.

8. Optical switches and routers

Optical switches and routers with low latency and low power consumption are also important building blocks for on-chip optical interconnection. Here, we discuss microresonator-based switches and routers, that were implemented using EO effect and thermo-optical (TO) effect.

8.1. EO switches using FCD effect

The key advantages of EO switching using the carrier-injection FCD effect include (i) sub-ns to ns tuning speed

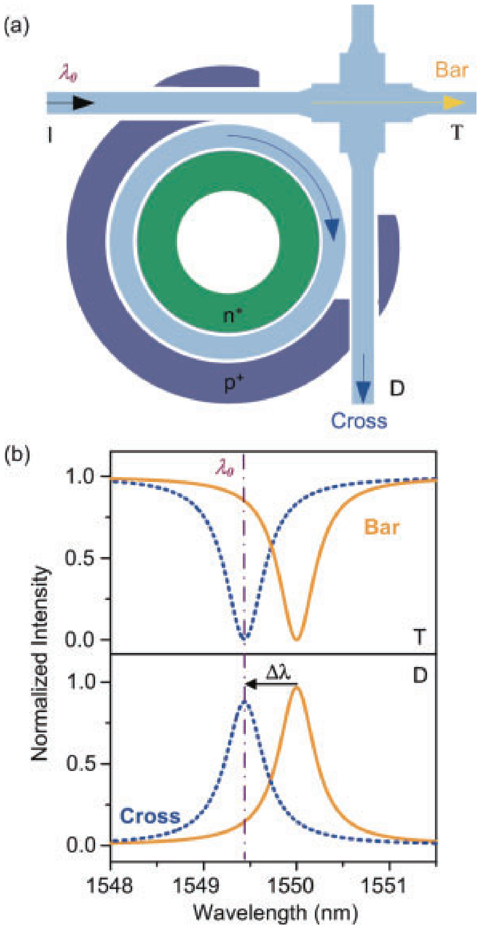

Figure 15 (online color at: www.lpr-journal.org) (a) Schematic of a silicon p-i-n diode embedded microring resonator-based switch coupled with a waveguide crossing. (b) Schematic of throughput- and drop-port transmission spectra. The carrier wavelength λ_0 is positioned at the off-resonance wavelength in the bar state and at the on-resonance wavelength in the cross state. I: input port. T: throughput port, D: drop port.

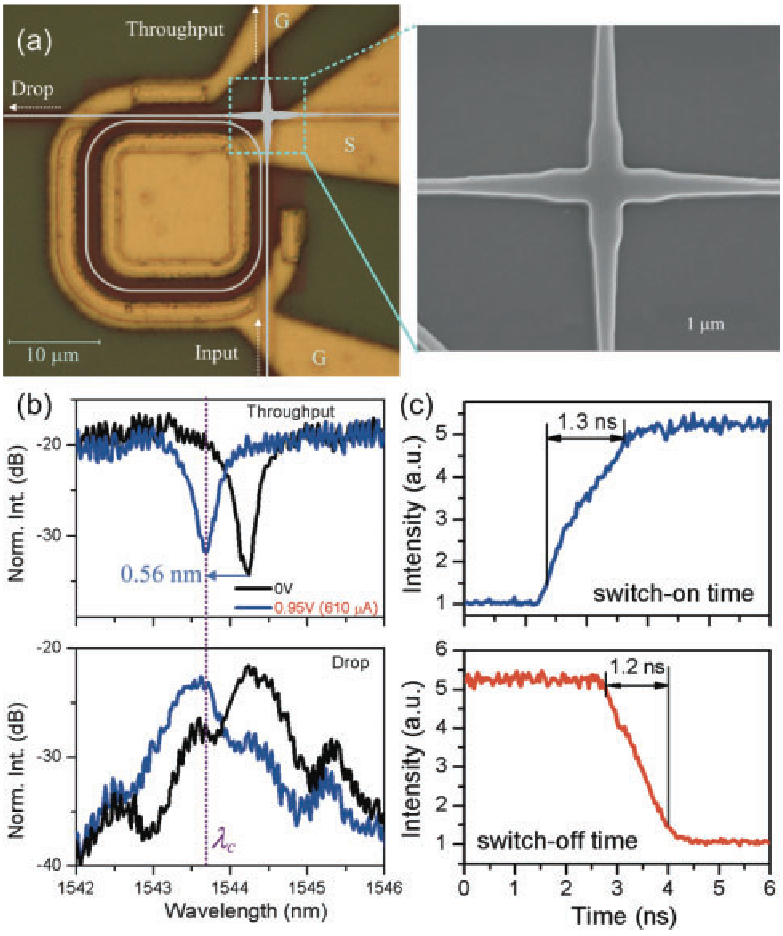

Figure 16 (online color at: www.lpr-journal.org) (a) Optical micrograph of a carrier-injection-type electro-optical switch using a microring resonator side coupled to a MMI waveguide crossing. The microring and the waveguide crossing are colored in gray. Metal-pad symbols: G: ground; S: signal. Inset: SEM of the MMI waveguide crossing. (b) Measured throughput- and drop-port transmission spectra upon drive voltages of 0 and 0.95 V. λ_c: carrier wavelength. (c) Measured switch transitions at the drop port showing nanosecond-speed 10-to-90% switch-on and 90-to-10% switch-off times. Reproduced with permission from [77], @ 2009 IEEE.

and (ii) ~ sub-mW to mW power consumption. However, the shortcoming of such EO switching is that the resonance wavelength tuning range is practically limited due to the presence of FCA loss. For instance, a 2×10^{19} cm^{-3} injected carrier concentration induces ~ 2 nm spectral blueshift and 100 dB/cm FCA loss according to Eqs. (13) and (14). Given an optical microresonator with a Q factor of 5000 before carrier injection, the FCA loss degrades the Q factor to ~ 3000 and changes the ER.

Figure 15 illustrates the EO switch assuming the carrier-injection FCD effect. The p-i-n diode integrated microring resonator is side coupled to a waveguide crossing, as shown in Fig. 15a. A carrier wavelength λ_0 positioned at a normally off-resonance wavelength propagates to the throughput port as a bar-state, while λ_0 is routed to the drop port as a cross-state with the blueshifted resonance aligned at λ_0 upon carrier injection, as shown in Fig. 15b.

Previously, our group demonstrated such an EO switch [77]. We adopted the MMI-based waveguide crossing [78, 79]. The MMI waveguide design enables self-focusing of the guided mode at the crossing junction, and thus reduces scattering-induced radiation loss and crosstalk of the crossing.

Figure 16a shows the top-view optical micrograph of the EO switch [77]. The inset shows the SEM of the MMI crossing. The crossing exhibited 0.12 dB insertion loss and –40 dB crosstalk [78, 79]. Figure 16b shows the measured throughput- and drop-port transmission spectra in the vicinity of a resonance under 0 V and 0.95 V forward bias [77]. The resonance shows a 3-dB bandwidth of 50 GHz and an ER of 15 dB. The resonance wavelength was blueshifted by 0.56 nm (exceeding the linewidth) upon 0.95 V forward bias, which requires a dc power consumption of 600 µW. Figure 16c shows the measured 10-to-90% switch-on time and 90-to-10% switch-off time were 1.3 and 1.2 ns, respectively [77].

Besides the FCD effect, EO tuning using liquid crystals (LC) as an electro-optical tunable upper-cladding layer on a silicon-based microresonator has been proposed and studied. The key advantages of EO switching using LC as an upper cladding include (i) wide wavelength tuning range due to the typically large LC birefringence (results in up to ~ 25nm resonance wavelength tuning based on our previous study [80]) and (ii) low electrical power consumption due to the field effect in rotating the LC molecules. The switching time, however, is relatively slow in the range of tens of μs to ms, depending on the LC material and the cell design.

EO tunable LC-clad silicon microring resonators have been demonstrated with horizontal [81] and vertical [82] electrodes. The tuning efficiency is of the order of 0.01 nm/V. Compared with the FCD effect, the LC approach imposes an order-of-magnitude higher drive voltage. Previously, our group and collaborators also proposed and patented a photoaligned LC-clad silicon microresonator-based EO switch [80]. The novelty there involves the use of photoaligned LC instead of the conventional alignment methods.

8.2. TO switches

The silicon refractive index can also be changed with temperature variation. TO switching has the key merit of wide wavelength tuning range. The silicon thermally induced refractive-index change is $\sim 1.86 \times 10^{-4}\,\mathrm{K}^{-1}$ and absorption coefficient change is $\sim 10^{-4}\,\mathrm{cm}^{-1}\,\mathrm{K}^{-1}$ at 1550 nm [30]. For example, in order to tune the resonance wavelength by 10 nm, the temperature rise in silicon needs to be ~ 100 K, and the resulting induced loss is ~ 0.04 dB/cm, which is negligible. However, the tuning speed is typically of the order of μs due to slow thermal diffusion process.

The typical approach to control the silicon microresonator temperature is to integrate a microheater on the top. Figure 17a shows the top-view and cross-sectional schematics of a microheater-integrated microresonator [83]. The metal, typically Ti/Ni, was fabricated on top of the optical waveguide and along the microresonator circumference. In this particular device, the resonance wavelength tuning efficiency was estimated as 0.3 nm/mW [83], as shown in Fig. 17b. Figure 17c shows the measured tuning rise and fall times of 7 and 14 μs [83].

TO tuning efficiency was enhanced with opened air trenches on the two sides of the ring waveguide [84]. By trapping the heat in the waveguide regions, the air trenches improved the tuning efficiency to 0.9 nm/mW. The tuning efficiency was further improved to 4.8 nm/mW by removing the undercladding underneath the microring waveguide, thus forming a free-standing microresonator [85]. However, due to the heat trapping, the tuning time was an order of magnitude longer than that for the device without undercuts.

The tuning speed has also been improved by optimizing the microheater integrated waveguide structure [86,87]. The vertical separation between the waveguide and the microheater was optimized in order to efficiently couple heat into the waveguide while minimizing the absorption loss due to the metal heater. The cladding material can be changed from commonly used SiO_2 to SiN, which has a higher thermal conductivity.

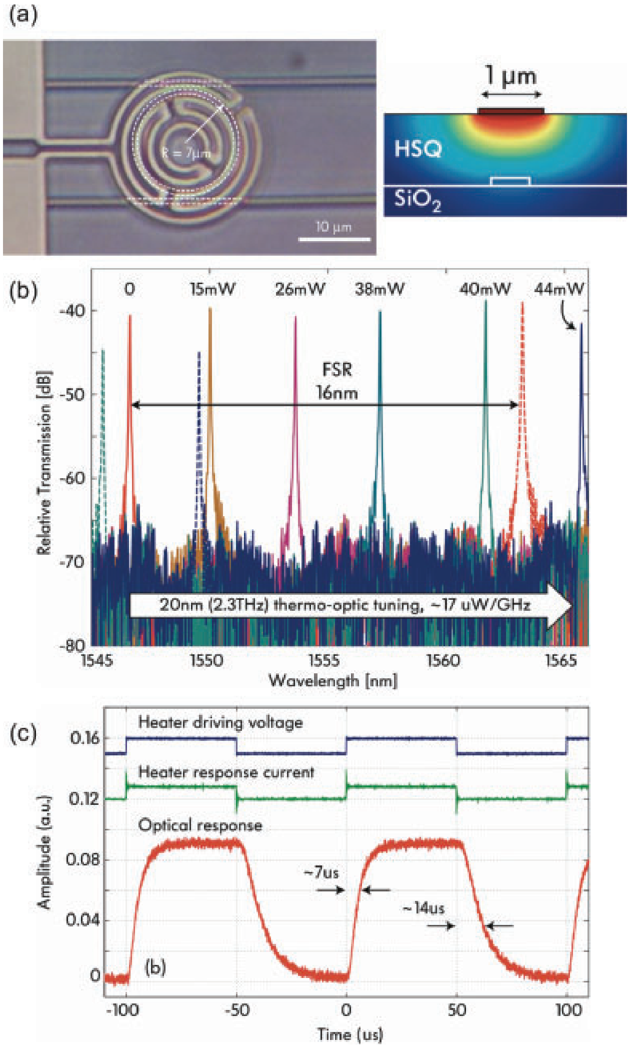

Figure 17 (online color at: www.lpr-journal.org) (a) Top-view optical micrograph of a silicon microring resonator integrated with a microheater. Inset: Numerically simulated temperature distribution in the upper cladding underneath the microheater. HSQ: hydrogen silsequioxane. (b) Measured drop-port transmission spectra upon various electrical tuning powers. (c) Measured optical response upon thermal tuning showing a 7-μs rise time and a 14-μs fall time. Reproduced with permission from [83], ©2007 IEEE.

Other than integrating a microheater on top of the waveguide, the microresonator can also be directly heated with current injection [88]. The direct heating showed a relatively efficient 0.55 nm/mW tuning efficiency with a relatively short switching time of 1 μs. However, such an embedded heater approach suffers additional optical loss and imposes complicated fabrication process.

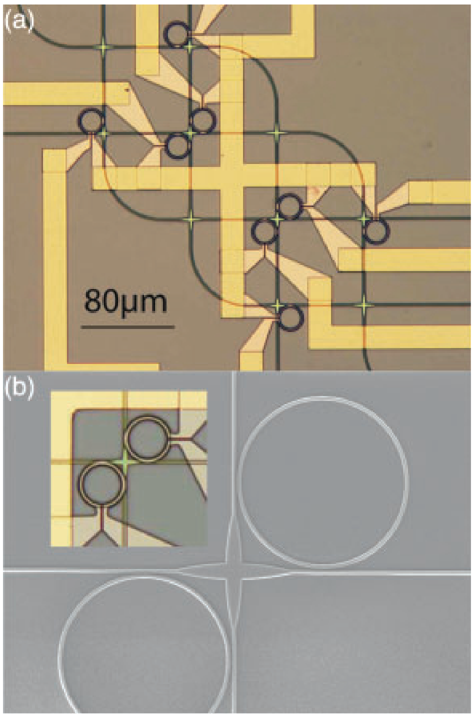

Figure 18 (online color at: www.lpr-journal.org) (a) Optical micrograph of a 4×4 nonblocking silicon optical switch using the themo-optical effect. (b) SEM of the waveguide crossing and coupled microring resonators. Inset: optical micrograph of the microring switch with microheaters. Reproduced with permission from [86], @ 2008 OSA.

8.3. Optical routers

The EO or TO switches integrated in a network topology constitute an on-chip optical router. The detailed discussion on this topic can be found in a review article by our group [77]. Here, we highlight two representative microresonator-based optical routers.

Sherwood-Droz et al [86] demonstrated a 4×4 nonblocking silicon optical router using TO switching. Figure 18a shows the optical micrograph of the device comprising eight microring resonators and ten waveguide crossings, with a footprint of 0.07 mm^2 [86]. Figure 18b shows the SEM of the waveguide crossing and the coupled microring resonators [86]. The insertion loss of each crossing was shown to be 0.51 dB. Their design enabled bidirectional communications among the four input ports and the four output ports. Each communication path demonstrated a maximum ER of 20.79 dB and a bandwidth of 38.5 GHz.

The shortcomings of such optical routers are relatively slow switch on/off times, of the order of μs, and relatively high power consumption for the resonance wavelength tuning (0.25 nm/mW in Sherwood-Droz et al [86]). Moreover, in a two-dimensional mesh/torus network, additional ports for data injection and ejection are necessary. A 5×5 nonblocking optical router is required.

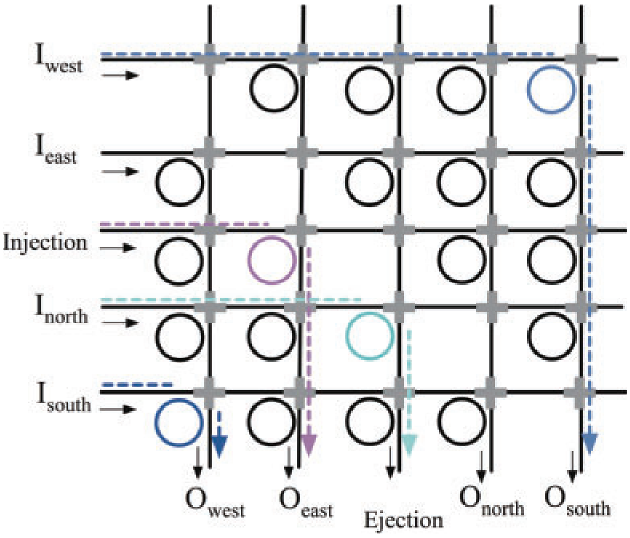

Figure 19 (online color at: www.lpr-journal.org) Schematic of a 5 × 5 optical router comprising 20 identical microring resonator-based switch elements coupled to a MMI crossing grid array with 25 crossings. The dashed arrows illustrate some of the possible light paths with the colored microrings correspond to the cross state. Reproduced with permission from [77], @ 2009 IEEE.

Our group proposed a 5×5 silicon microring resonator based EO optical router [77]. Figure 19 illustrates the data paths in the proposed optical router [77]. The router comprises 5 input ports and 5 output ports, enabling simultaneous bidirectional communications in four orthogonal directions including data injection and ejection. Each data path connecting one input port to one output port is established by switching on one microring resonator. Multiple data paths can be established simultaneously. The router is nonblocking.

For proof-of-concept, we demonstrated an EO 2×2 optical router [77].

Figures 20a and b show the optical micrograph of the device and a schematic of the data paths in the router [77]. Figures 20c and d show the measured transmission spectra with the light separately launched from ports I1 and I2 [77]. The 3-dB bandwidth for the four microrings was ∼ 65 GHz. Due to fabrication imperfections, however, the resonance wavelengths were misaligned, which imposes additional dc power consumption (within 300 μW) for compensating the resonance wavelength misalignment.

9. Coherent control of resonance lineshapes

Resonance lineshape tuning by means of coherent interference provides additional functionalities. There are three common schemes proposed and demonstrated in silicon microresonators, namely i) coherent interference between a microresonator resonance and a nonresonant background, as in Fano resonances [89], ii) coherent interference between a microresonator resonance and a detuned microresonator resonance, as in electromagnetically induced transparency (EIT) [90] and iii) coherent interference between a microresonator resonance and a coherent feedback [91].

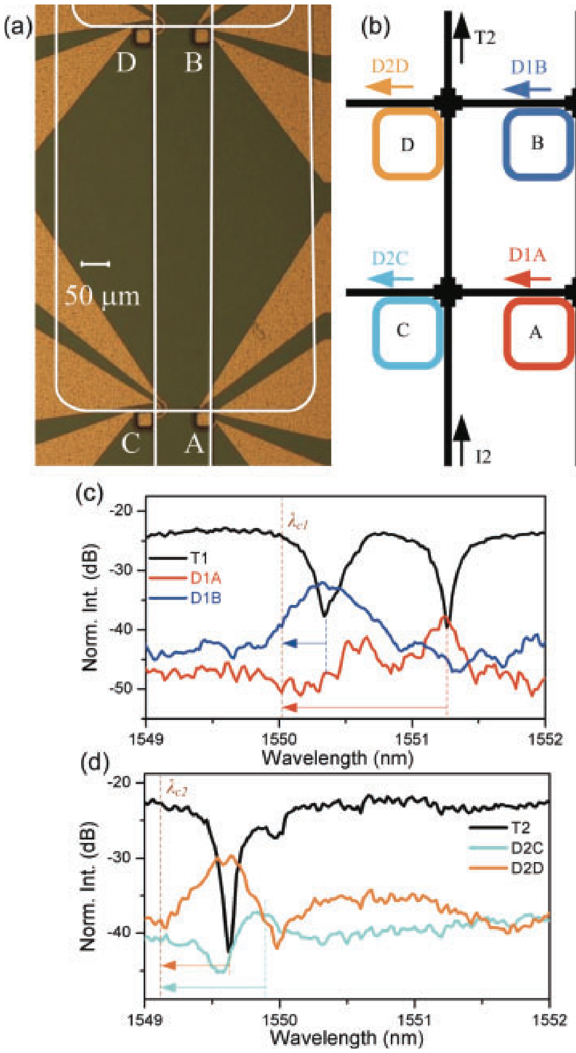

Figure 20 (online color at: www.lpr-journal.org) (a) Optical micrograph of a 2 × 2 microring resonator-based switch matrix. (b) Schematic of the switch matrix illustrating two input ports I1 and I2, two throughput ports T1 and T2, two drop ports D1A and D1B for I1 and two drop ports D2C and D2D for I2. (c) Measured throughput- and drop-port transmissions at ports T1, D1A and D1B when light was launched from input port I1. (d) Measured throughput- and drop-port transmissions at ports T2, D2C and D2D when light was launched from input port I2. Reproduced with permission from [77], @ 2009 IEEE.

(i) Resonance interference with a coherent background

Figure 21a shows one proposed configuration comprising a silicon microring resonator coupled with a MZI [89]. The resonance pathway corresponds to the lightwave propagating in the microresonator-coupled MZI arm, and the coherent background pathway corresponds to the amplitude-split lightwave propagating in the MZI reference arm. The two lightwaves recombine at the MZI output ports.

Figure 21b shows the measured transmission spectra for the two output ports [89]. Both port-1 and port-2 transmission spectra exhibited asymmetrical Fano resonance lineshapes. The lineshapes can be controlled by modulating the phase in the MZI reference arm.

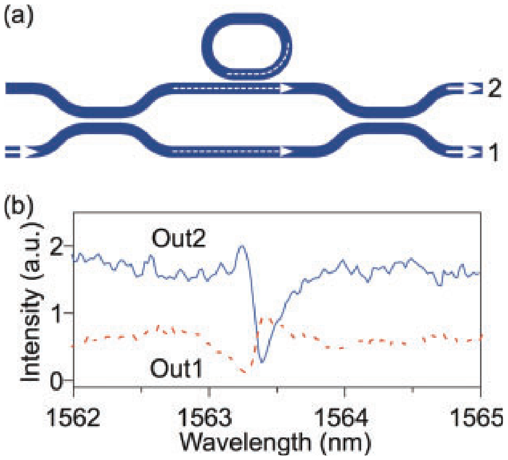

Figure 21 (online color at: www.lpr-journal.org) (a) Schematic of a MZI-coupled microring resonator. Dashed arrows illustrate the coherent light paths. (b) Measured transmission spectra at output port 1 (red dashed) and port 2 (blue solid) showing asymmetric Fano lineshapes. Reproduced with permission from [89], ©2007 OSA.

The sharp asymmetrical lineshapes can find applications in biosensing [92, 93]. The MZI-coupled microring resonators have also been proposed for tailoring the filter lineshape with a flat-top and box-like spectral response [94, 95].

(ii) Resonance interference with a coherent resonance

Like Fano resonances, EIT-like phenomenon can occur in a microresonator system in which two coupled microresonators coherently interfere. Figure 22a shows the top-view optical micrograph of such a silicon double-ring microresonator device [90]. The coherent lightwave from the two slightly detuned microresonators destructively interfere at the throughput port.

Figure 22b shows the measured and modeled transmission spectra at the throughput port [90]. A transparency window with a full width at half-maximum (FWHM) of 0.13 nm was observed in the transmission dip with FWHM of 4.4 nm. Such silicon coupled microring resonator structures with EIT-like lineshapes have found applications in optical delay lines (see Sect. 10).

(iii) Resonance interference with a coherent feedback

The resonance lineshape can also be enhanced or suppressed by means of interference with a coherent feedback.

Figure 23a shows the schematic of a silicon feedback-coupled microring resonator [91]. By tuning the feedback phase and amplitude, say using the FCD effect, we can enhance or suppress the resonance. Figure 23b shows the measured and modeled transmission spectra [91]. While the resonance wavelengths were almost fixed upon the three different feedback phase values $\delta\varphi$ (controlled upon carrier injection across the feedback path), the resonance lineshape (resonance C) varied significantly with only slight variations in the resonance

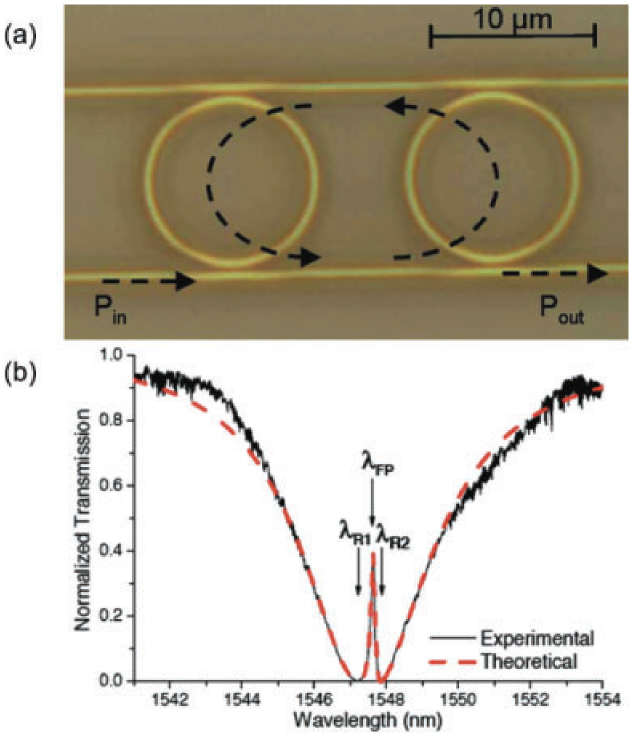

Figure 22 (online color at: www.lpr-journal.org) (a) Top-view optical micrograph of a double-ring resonator laterally coupled with two parallel waveguides. Dashed arrows indicate the light coupling between the two slightly detuned microring resonators. (b) Measured (black solid) and theoretical (red dashed) throughput transmission spectra revealing EIT-like resonance lineshape. Reproduced with permission from [90], ©2006 OSA.

Q values. Nonetheless, such coherent feedback control highly depends on the resonance wavelength. Thus, the resonance lineshape modulation varies among resonances (e.g. resonances A and B were relatively less affected by the feedback interference).

It is conceivable that the feedback-microring that enables controlled resonance lineshape tuning with a large dynamic on-off ratio offers more functionalities than simple waveguide-coupled microring resonators. Previously, we have also proposed that the microring resonance wavelength can be separately tuned by modulating the microring round-trip phase. Such functionality has been used for reconfigurable filters [91, 96, 97], switches and modulators [98, 99].

10. Optical delay lines

Optical delay lines are another key component for on-chip optical interconnects. The traditional way to obtain optical delay is by passing the light through a dispersive medium. Other than relying on a strongly dispersive medium, the strong dispersion can be obtained from microresonator-based structures (see Sect. 2). Table 3 summarizes the state-of-the-art of the microresonator-based optical delay lines on silicon chips. The key performance metrics for the optical delay lines are time delay, bandwidth, insertion loss and delay tunability. The figure-of-merit is the delay-bandwidth product (DBP).

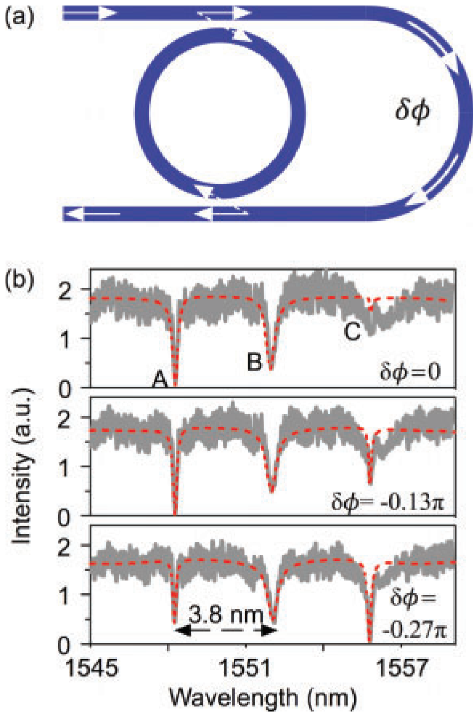

Figure 23 (online color at: www.lpr-journal.org) (a) Schematic of a feedback-coupled microring resonator. Arrows indicate the light trajectories and the feedback path. $\delta\varphi$: feedback phase. (b) Measured (gray solid) and modeled (red dashed) transmission spectra upon $\delta\varphi = 0$, -0.13π, and -0.27π. Resonance C shows pronounced resonance lineshape tuning as a function of $\delta\varphi$. Reproduced with permission from [91], ©2007 OSA.

10.1. Microring-based optical delay lines

The waveguide-coupled microring resonator exhibits time delay/advance depending on the coupling regimes (see Sect. 2). Thus, the time delay and advance can be tuned by controlling the coupling regimes. Recently, we reported microring resonator-based EO tunable delay lines [100].

Figure 24a shows the optical micrograph of a racetrack microring resonator integrated with a lateral p-i-n diode on a SOI substrate [100]. Figures 24b–d show the measured transmission spectra, time delay, and deduced optical phase responses upon various bias voltages and injection currents [100]. Upon forward biasing the p-i-n diode, carrier injection increased the microring FCA loss and thus tuned the coupling regime from overcoupling to undercoupling, and correspondingly tuned from time delay to time advance. The single microring resonator-based tunable delay lines have also been demonstrated using the TO effect [101].

However, the tunable time delay demonstrated in this work was accompanied with resonance wavelength shifts. In order to separate the time delay tuning from the resonance wavelength shifts, our group recently demonstrated a

Table 3 Key measured performances of microresonator-based optical delay lines on silicon chips.

Structure	Material	N	Delay (ps)	Bandwidth (GHz)	DBP	Insertion loss (dB)	Ref.
Single element	SOI	1	95	3.5	0.3	40	[100]
	SOI	1	80	5	0.4	28	[101]
	SOI	1	84	1.5	0.132	38	[102]
EIT	SOI	2	25	–	–	–	[90]
	SOI	2	29	–	–	30	[103]
SCISSOR	SOI	56	510	54	27	25	[14]
	Hydex	8	2,483	2.5	6	6	[106]
		32	357	40	14	10	
CROW	SOI	100	220	–	–	26	[14]
	SOI	235	145	625	90	19	[109]
	SiON	8	800	6.25	5	8	[110]
	SiN	101	110	18.75	2	50	[111]

N: number of cascaded microresonators. DBP: delay–bandwidth product.

feedback-microring tunable delay lines by controlling the coupling regime via tuning the feedback phase and loss, while the resonance wavelength can be separately tuned.

Figure 25a shows the optical micrograph of the fabricated device comprising the feedback-microring resonator connected to a control microring resonator without the feedback waveguide [102]. The principle of the feedback-microring resonator is discussed in Sect. 9. By forward biasing the diode U across the feedback waveguide with voltage V_U, we can control the transmission intensity and phase response of the device and thereby tune the time delay/advance at a fixed resonance wavelength. By forward biasing the diode A across the microring with voltage V_A, we can blueshift the resonance wavelength.

Figures 25b–d and e–g show the measured transmission spectra and corresponding time delay/advance at three different resonance wavelengths upon various bias voltages [102]. The feedback-microring resonator showed a delay bandwidth (FWHM delay) of ~ 1.5 GHz at the maximum delay of 84 ps, suggesting a DBP of ~ 0.132. In comparison, our previously demonstrated device of a single waveguide-coupled microring resonator showed a delay bandwidth of ~ 3.5 GHz with a maximum delay of 95 ps, which gave a DBP of ~ 0.3 [100]. Other silicon single microring resonator-based devices have demonstrated a DBP of ~ 0.4, albeit using transmission intensity bandwidth [101].

One shortcoming of the above approaches using notch filters is that the optical delay within the resonance dip suffers low transmission intensity. In order to enable high transmission intensity while exhibiting strong optical delays, optical delay lines utilizing an EIT-like lineshape that exhibits strong dispersion at the transmission resonance peak within the broad transmission dip (see Sect. 9) [90] have been considered. The EIT-like lineshape and the resulting time delay were attained in a double-microring resonator system coupled to two parallel waveguides on a SOI substrate (see Fig. 22) [90]. The EIT-like lineshape and time delay/advance were also observed using a single microring resonator with clockwise (CW)-counterclockwise (CCW) modes mutual coupling induced mode splitting [103].

10.2. Cascaded microresonators-based optical delay lines

Nonetheless, both the Lorentzian and EIT-like resonance lineshapes exhibit narrowband transmissions, which are not suitable for high-speed data transmissions. In order to increase the bandwidth of the optical delay lines, cascaded microresonators have been investigated, namely side-coupled integrated sequence of spaced optical resonators (SCISSORs) and coupled-resonators optical waveguides (CROWs).

SCISSORs utilize cascaded multiple microresonators coupled in series to a common bus waveguide (see Fig. 26a) [14, 104–106]. As the light propagates inside each of the microresonators for multiple round-trips and passes to the next microresonator, the group delay is significantly enhanced. There is no mutual coupling among the microresonators in SCISSORs.

CROWs utilize cascaded multiple microresonators in parallel. The light propagating inside a CROW can be coupled back and forth among all the microresonators, and thus results in intercavity coupling-induced bandwidth broadening and delay enhancement.

The first 100-microring CROW on a SOI substrate was demonstrated in 2007 [14].

Figure 26b shows the SEM of the CROW. The device demonstrated a maximum delay of ~ 220 ps with a footprint of only $\sim 0.045\,\mathrm{mm}^2$. Nonetheless, the demonstrated transmission profile showed significant ripples owing to the finite-size effect, which in principle can be mitigated by adopting different coupling strengths between the microresonator and the coupled waveguide from the intercavity coupling [107].

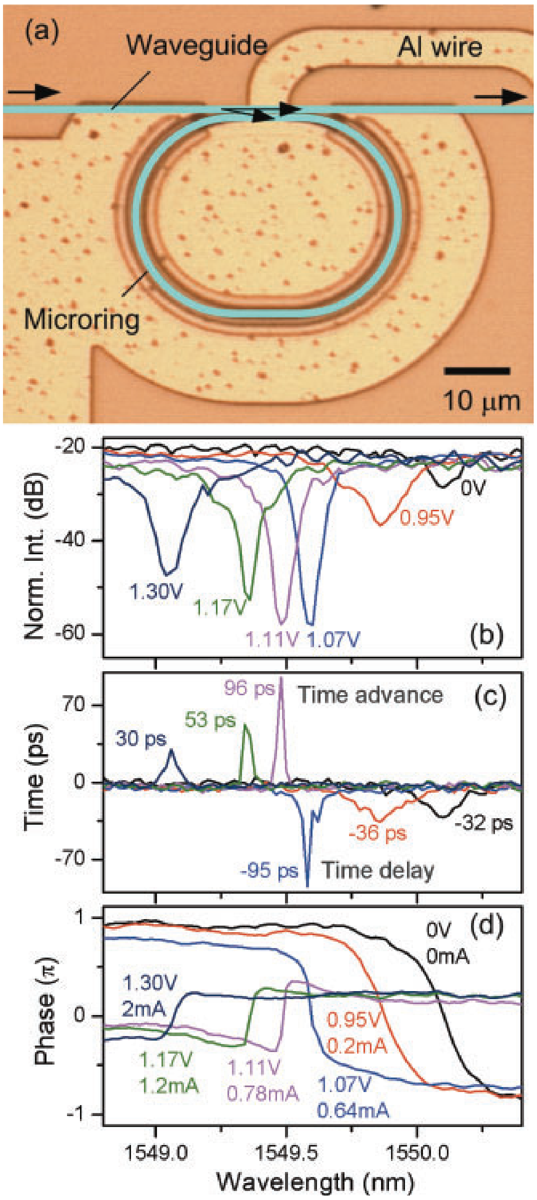

Figure 24 (online color at: www.lpr-journal.org) (a) Optical micrograph of a racetrack microresonator-based notch filter with a laterally integrated p-i-n diode on a SOI substrate. (b)–(d) Measured (b) transmission spectra, (c) time delay/advance and (d) deduced optical phase response upon various bias voltages and injection currents. Reproduced with permission from [100], @ 2010 OSA.

Another issue with cascaded microresonators is fabrication-imperfection-induced structure disorder. Anderson localization has been observed in a CROW with up to 100 cuboidal microresonators on a SOI substrate (Fig. 26c) [108]. Optimization and precision fabrication of CROW structures is of the essence for realistic optical delay lines applications.

Recently, Cooper et al [109] have demonstrated a 235-microring CROW and showed 145 ps delay. To our knowledge, this is the longest CROW device ever demonstrated using silicon microring resonators.

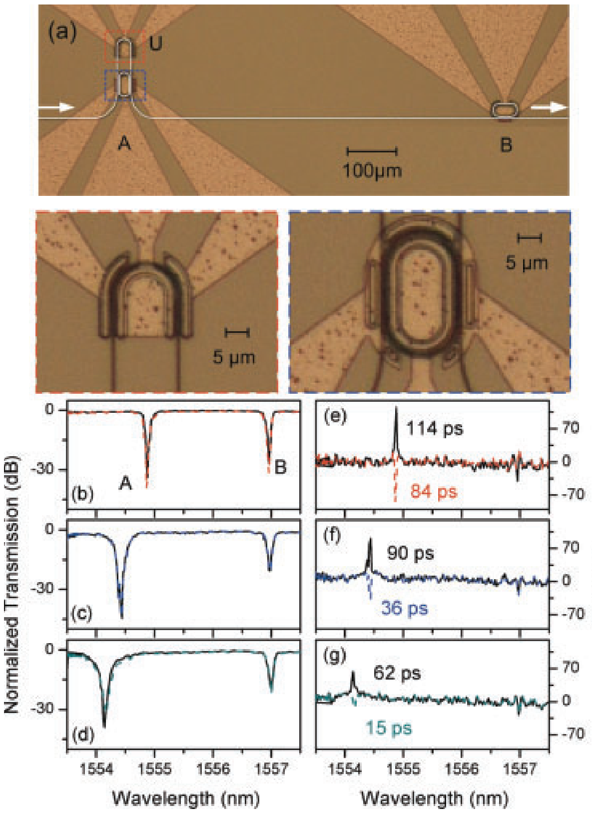

Figure 25 (online color at: www.lpr-journal.org) (a) Optical micrograph of the feedback-microring resonator connected to a microring-resonator-based notch filter without feedback waveguide. Insets: Zoom-in micrographs of the feedback waveguide (red) and the microring resonator (blue). Measured (b)–(d) transmission spectra and (e)–(g) corresponding time delay and advance. (b), (e) $V_A = 0.00$ V, $V_U = 1.07$ V (black), $V_U = 1.10$ V (red dashed); (c), (f) $V_A = 0.95$ V, $V_U = 1.31$ V (black), $V_U = 1.34$ V (blue dashed); (d), (g) $V_A = 1.00$ V, $V_U = 1.49$ V (black), $V_U = 1.59$ V (green dashed). Reproduced with permission from [102], @ 2011 OSA.

The delay tunability of the microring CROW delay lines has also been attained [110]. The delay value depended on the reconfigurable number of the microring resonators that were aligned to the signal carrier wavelength. With each of the microrings providing 50 ps delay, the CROW delay lines with 6 microrings showed delay tuning range from 0 ps to 300 ps.

Although cascaded microresonator arrays can enhance the group delay, there are two major issues for such array structures. First, conventional microring/microdisk resonators rely on evanescent coupling for interresonator couplings and coupling with bus waveguides. The nanofabrication of many submicrometer-sized gap separations with high uniformity is technologically challenging. Secondly, the large number of cascaded microresonators also tends to increase the insertion loss.

Previously, based on the demonstrated microspiral- and double-notch-shaped microdisk resonators (see Section V), our group proposed a CROW structure with gapless-coupled

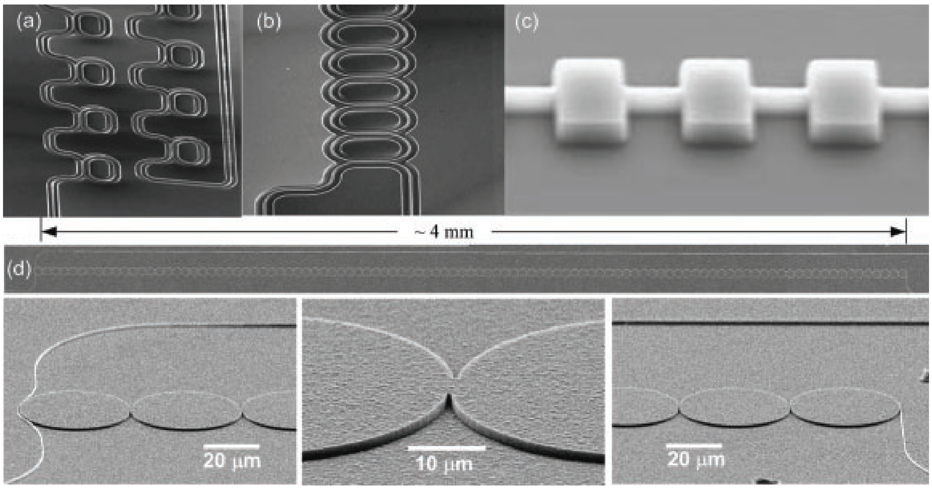

Figure 26 (online color at: www.lpr-journal.org) Cascaded microresonator-based optical delay lines. (a) SEM of a 56-element cascaded all-pass filter with each silicon microring resonator coupled to the same bus waveguide. Reproduced with permission from [14], @ 2007 NPG. (b) SEM of a CROW structure with 100 cascaded silicon microring resonators. Reproduced with permission from [14], @ 2007 NPG. (c) SEM of a single-mode waveguide periodically loaded with 100 silicon square-shaped microdisk resonators. Reproduced with permission from [108], @ 2008 NPG. (d) SEM of a CROW structure with 101 cascaded spiral-shaped and double-notch-shaped SiN microdisk resonators. The zoom-in SEMs show the input-coupling region, the intercavity coupling region and the output-coupling region. Reproduced with permission from [111], @ 2009 OSA.

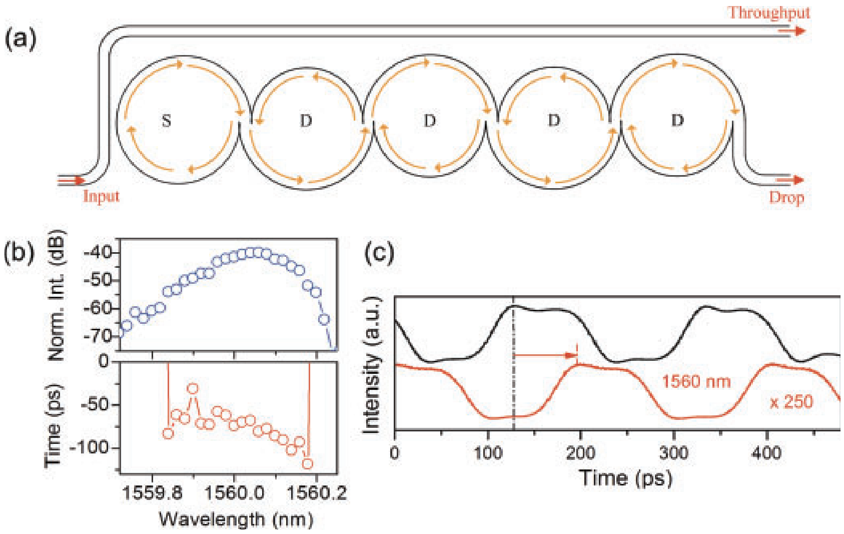

Figure 27 (online color at: www.lpr-journal.org) (a) Schematic of the CROW structure using gapless-coupled microdisk resonators. S: microspiral microdisk, D: double-notch-shaped microdisk. (b) Measured transmission spectrum and time delay of the 101-element CROW within the transmission band. (c) Measured 10-Gbit/s PRBS ($2^{10}-1$) data transmission showing ~ 63 ps time delay at 1560 nm (red waveform) relative to an off-resonance wavelength (black waveform). Reproduced with permission from [111], @ 2009 OSA.

microdisk resonators in order to avoid the interresonator coupling gap spacing [111].

Figure 27a shows a schematic of the CROW with gapless-coupled microdisks [111].

Figure 26d shows the SEM of the 101-element gapless-coupled microdisk CROW [111].

Figure 27b shows the measured transmission spectrum and time delay of the 101-element CROW within a transmission band of 0.35 nm [111]. The measured optical delay at the band center was ~ 70 ps, while the delay was ~ 110 ps near the band edge. Our measurement suggested ~ 0.2 dB/disk insertion loss [111], which we attributed largely to the scattering loss at the joint notches.

Figure 27c shows the measured 10 Gbit/s PRBS ($2^{10}-1$) signal waveforms in the drop-port transmission at the band-center wavelength (1560 nm) and in the throughput transmission at an off-resonance wavelength, indicating a time delay of ~ 63 ps at the band center [111].

11. Subbandgap wavelength-selective p-i-n photodetectors

Microresonator-based p-i-n photodetectors have a resonant-cavity-enhanced (RCE) field, and thus offer enhanced responsivity and wavelength selectivity at resonance wavelengths. In the context of on-chip optical interconnections, such wavelength-selective photodetectors can then discern particular WDM channels without employing an additional wavelength channel filter or demultiplexer. The detailed discussion on subbandgap absorption mechanisms can be found in Sect. 3.

11.1. Defect-state absorption-based p-i-n photodetectors

Previously, we demonstrated an all-silicon subbandgap RCE p-i-n photodetector (RCE-PD) in a microring resonator with SSA (see Sect. 3) at 1550 nm wavelengths [112]. Figure 28a shows the optical micrograph of the fabricated microring resonator-based p-i-n photodetector [112]. Figure 28b shows the measured throughput transmission spectrum revealing resonances with a Q factor of 8000 [112]. Figure 28c shows the correspondingly measured wavelength-selective photocurrent spectrum across the embedded p-i-n diode [112]. We observed an on-resonance photocurrent with a 20-fold enhancement compared with an off-resonance photocurrent. The on-resonance responsivity was around 0.12 mA/W upon 0 V bias and 0.25 mA/W upon –15V bias. The responsivity was, however, relatively low mainly due to the weak SSA process.

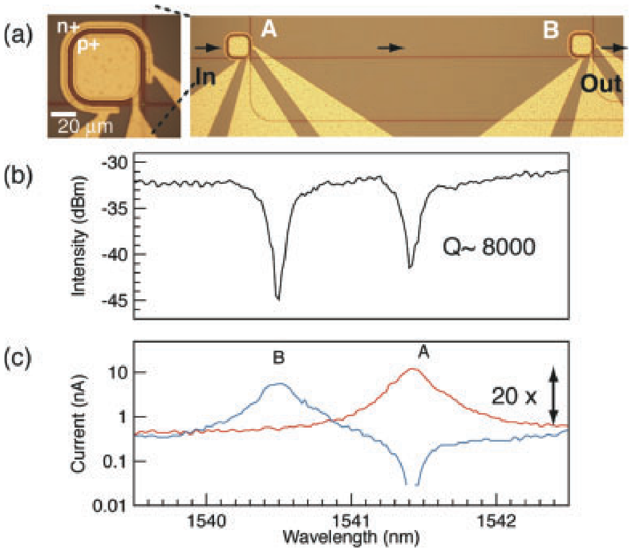

Figure 28 (online color at: www.lpr-journal.org) (a) Optical micrograph of two serial-cascaded microring resonators integrated with p-i-n diodes. Inset: Zoom-in micrograph of the microring resonator. (b) Measured throughput-port transmission spectrum. (c) Measured photocurrent spectrum from the p-i-n diodes of microring resonators A (red) and B (blue). Reproduced with permission from [112], ©2009 AIP.

With a higher absorption coefficient attained by increasing the density of defect states in the silicon waveguide, Doylend et al [113] recently demonstrated a silicon RCE-PD with 0.14 A/W responsivity upon –10 V bias, with sub-0.2-nA leakage current. Figure 29a shows the schematic of their racetrack microring resonator integrated with a defect-state-rich waveguide section [113]. The defect states were formed by boron implantation into a 60-µm long waveguide section inside the racetrack microring resonator. These implanted defect states provided better spatial overlap with the waveguide mode, compared to naturally formed waveguide surface defect states, enabling 10 dB/cm absorption. Figure 29b shows the measured photocurrent responsivity spectrum [113]. The RCE-PD showed comparable performance to the silicon waveguide PD [114, 115], albeit with a 50-fold reduction in the diode size. Together with TO resonance wavelength tuning, the silicon RCE-PD thus functioned as a tunable wavelength-selective photodetector.

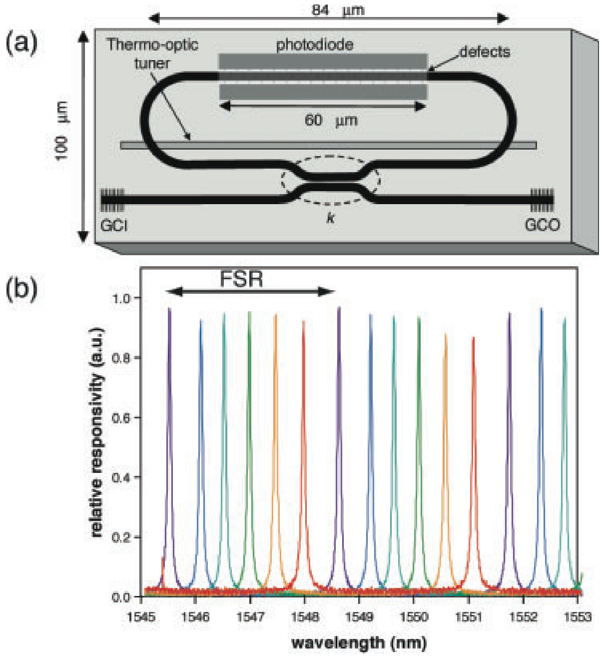

Figure 29 (online color at: www.lpr-journal.org) (a) Schematic of a p-i-n diode integrated racetrack microresonator with implantation-induced defects. (b) Measured responsivity as a function of wavelength upon various thermally tuned resonance wavelengths. Reproduced with permission from [113], ©2010 OSA.

Recently, Preston et al [116] demonstrated the cavity-enhanced defect-state-based subbandgap PD using a deposited polycrystalline silicon microring resonator. The polycrystalline silicon waveguide exhibited a 6-dB/cm absorption loss. Using a microring resonator with $Q \sim 10\,000$, their PD attained a subbandgap responsivity of 0.15 A/W upon bias voltage of –13 V.

11.2. TPA-based p-i-n photodetectors

Besides, TPA (see Sect. 3) has also been proposed as an alternative subbandgap absorption mechanism to realize all-silicon on-chip photodetection. As TPA is a relatively weak nonlinear optical process, previously demonstrated TPA-based photodetection using a relatively large-sized ($> 1\,\mu m^2$) core waveguide requires long waveguide length and high input optical power [117]. Using a submicrometer-sized waveguide, Bravo-Abad et al [118] proposed to use

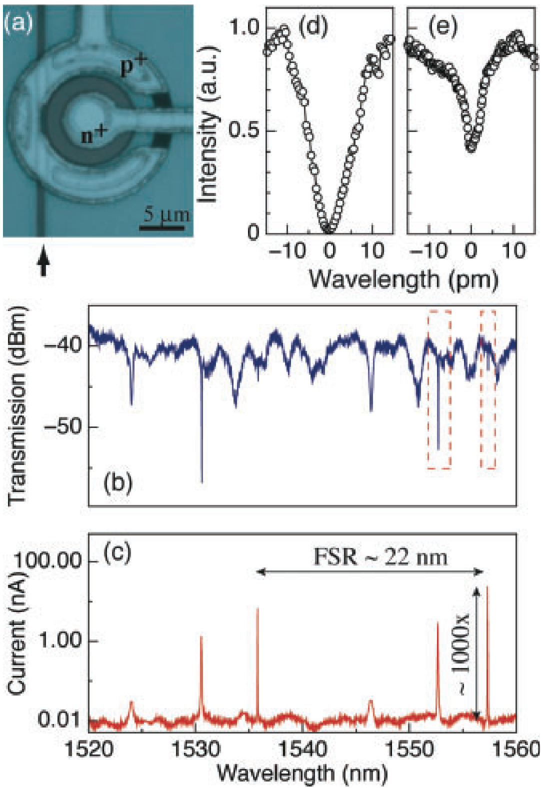

Figure 30 (online color at: www.lpr-journal.org) (a) Optical micrograph of a microdisk resonator integrated with a p-i-n diode. (b) Measured throughput-port transmission spectrum. (c) Measured photocurrent spectrum from the p-i-n diode. (d)–(e) High-resolution spectra of the two resonances shown in (b). Reproduced with permission from [46], ©2010 AIP.

all-silicon microring and photonic crystal cavities in order to enhance the TPA photodetection. They numerically studied the feasibility of ultrafast TPA-photodetection using microresonators with a Q factor of the order of 10^4.

Previously, our group utilized high-Q WGMs in a 10-µm diameter silicon microdisk resonator to demonstrate RCE photodetection using TPA at the 1550-nm wavelengths [46]. Figure 30a shows the optical micrograph of the fabricated microdisk resonator with an integrated p-i-n diode [46]. Figure 30b shows the measured transmission spectrum revealing multiple WGMs with a Q factor of the order of 10^5 [46]. Figures 30d–e show high-resolution spectra of two resonances in Fig. 30b (dashed-line boxes). Figure 30c shows the measured corresponding photocurrent spectrum upon 0 V bias across the p-i-n diode [46]. The photocurrents at resonance wavelengths exceed those at off-resonance wavelengths by up to three orders of magnitude. We demonstrated that the photocurrent generation efficiency in a silicon microdisk resonator outperforms that in a waveguide structure with several orders of magnitude longer p-i-n diode length [44].

12. Optical signal processing

Silicon microresonators have found applications in optical signal processing. The microresonator transmission intensity and phase response have been tailored for applications such as modulation format conversion [119], differential-phase-shift-key (DPSK) modulation [120], arbitrary waveform generation [121], temporal differentiator [122], frequency doubling [123] and phase shifters [124, 125]. Here, we highlight three representative examples, including format conversion, DPSK modulation and ultrabroad-bandwidth arbitrary radio-frequency (RF) waveform generation.

12.1. Format conversion

Our group demonstrated the nonreturn-to-zero (NRZ) to pseudoreturn-to-zero (PRZ) format conversion using a silicon microring resonator-based notch filter [119]. Figure 31a illustrates the format conversion. Figures 31b and c show the modeled optical waveform (Fig. 31b) and frequency spectra (Fig. 31c) of the NRZ signal and the converted PRZ signal. The optical carrier of the input NRZ signal is suppressed, while the high-frequency sidebands are passed by the notch filter. Thus, the NRZ signal is converted to the PRZ signal corresponding to the transition edges of the NRZ signal.

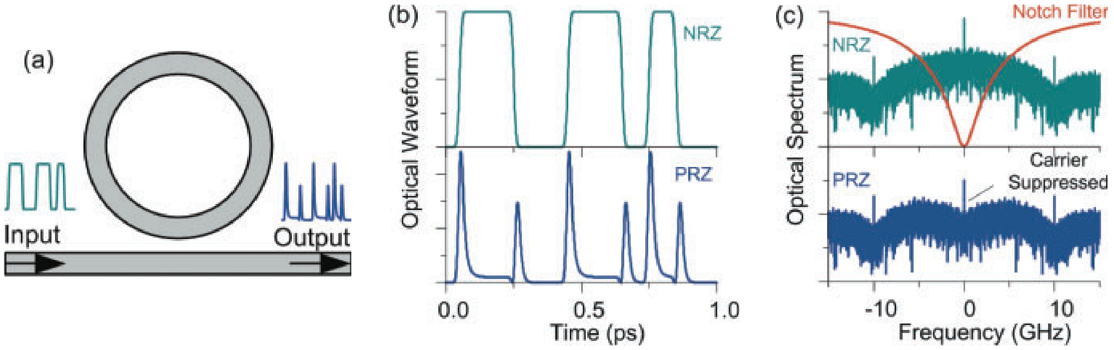

Figure 31 (online color at: www.lpr-journal.org) (a) Schematic of NRZ-to-PRZ format conversion using a microring- resonator-based notch filter. (b) Modeled waveforms of an input NRZ signal (green) and the converted PRZ signal (blue). (c) Modeled frequency spectra of the input NRZ signal (green) and the converted PRZ signal (blue). The frequency spectrum of the notch filter (red) is centered at the carrier wavelength.

12.2. DPSK modulation

The advanced DPSK modulation format can be attained using the phase response of a waveguide-coupled microring channel add-drop filter [120]. The filter throughput port generates the alternate-mark inversion (AMI) signal, and the filter drop port generates the dualbinary (DB) signal. The demodulation of DPSK was demonstrated using a silicon waveguide-coupled microring resonator throughput transmission [126].

12.3. Ultrabroad-bandwidth arbitrary RF waveform generation

An ultrabroad-bandwidth arbitrary RF waveform can be generated by using a silicon photonic chip-based spectral shaper [121]. Figure 32a shows the device schematic comprising eight cascaded feedback-microring resonators in an add-drop filter configuration [121]. The optical transmission spectrum can be controlled by thermally tuning both the resonant frequencies and the coupling strengths of the microring resonators. The optical frequency-domain spectrum was then converted into an electrical time-domain waveform via frequency-time mapping. Figure 32b shows an example of their generated RF waveform [121].

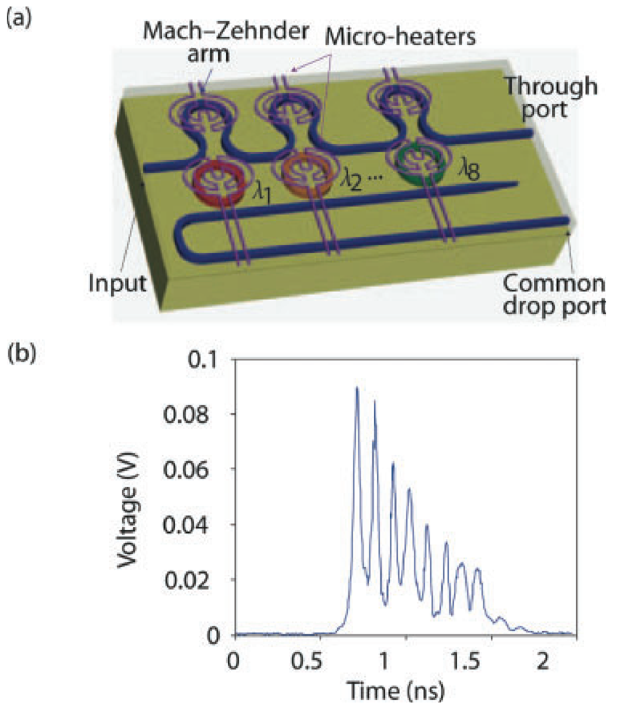

Figure 32 (online color at: www.lpr-journal.org) (a) Schematic of a silicon on-chip spectral shaper comprising cascaded feedback-microring resonators integrated with microheaters for broadband arbitrary RF waveform generation. (b) Measured 10-GHz electrical waveform controlled by the spectral shaper. Reproduced with permission from [121], ©2010 NPG.

13. Optical biosensing

Silicon microresonator-based optical biosensors have been attracting significant attention due to the key advantages of high sensitivity to refractive-index change (typically $\sim 10^{-4}$–10^{-5} RIU), compact size (tens of µm – ∼ 100 µm), and potential for large-scale integration in microfluidics applications. Here, we briefly discuss the sensing principle using microresonators. Figure 33a illustrates the cross section of a microring resonator-based sensor showing the resonance evanescent field extending outside the microring waveguide and interacting with the targeted biomaterial that is bound to the functionalized microring surface. Figure 33b shows the resonance wavelength shifts ($\Delta\lambda$) corresponding to the effective refractive-index change (Δn). The sensitivity of the effective refractive-index sensor is defined as $\Delta\lambda/\Delta n$, which is usually given as nanometer of resonance wavelength shift per refractive index unit (RIU). Figure 33c schematically shows the $\Delta\lambda$ varies linearly as a function of Δn. Thus, by monitoring $\Delta\lambda$, one can in principle detect the binding events and extract the targeted biomaterial concentration. The sensitivity and the detection limit are determined by $\Delta\lambda$ and the resonance linewidth $\delta\lambda$. The relation between $\Delta\lambda$, Δn and the effective microresonator size change ΔR due to the binding event is given as follows:

$$\frac{\Delta\lambda}{\lambda} = \frac{\Delta R}{R} + \frac{\Delta n}{n}. \qquad (15)$$

Microresonator-based biosensors have been realized using various structures including microrings [127–129], slot microresonators [130–132], microtoroids [133], and novel-shaped microresonators [134]. The following highlights some of the representative work. Table 4 summarizes the specification of the demonstrated silicon-based microresonator biosensors.

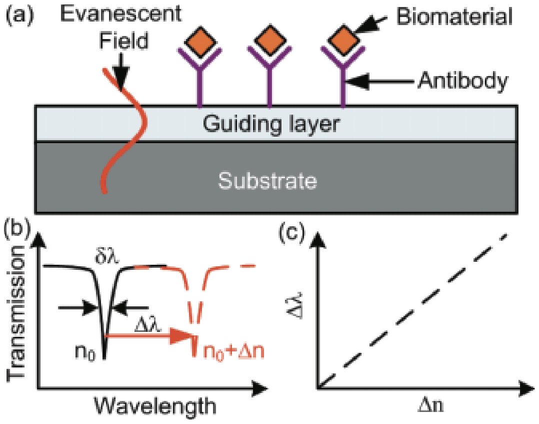

Figure 33 (online color at: www.lpr-journal.org) Schematic of the sensing principle of a microresonator-based biosensor. (a) Cross section of the microresonator device. The targeted biomaterials bind to the antibody, interact with the evanescent field and change the effective refractive index of the microresonator. (b) Resonance wavelength shifts upon an effective index change Δn induced by the binding events. (c) Schematic of the resonance wavelength shift $\Delta\lambda$ as a function of Δn.

Table 4 Key measured performances of microresonator-based optical biosensors on silicon chips.

Material	Structure	Dimensions	Q	Sensitivity/detection limit	Ref.
SOI	Racetrack	13 μm × 10 μm	20 000	avidin 10 ng/ml 0.37 fg mass	[127]
SOI	Microring	30 μm diameter	20 000	CEA protein 2 ng/mL	[128]
SOI	Folded microring	1.2 mm length 150 μm × 150 μm	19 600	Streptavidin protein 3 pg/mm^2 5 fg mass	[129]
SOI	Slot racetrack	13 μm × 10 μm 100 nm slot	330	298 nm/RIU 4.2×10^{-5} RIU	[130]
SiN	Slot microring	140 μm diameter 200 nm slot	1800	212 nm/RIU 2×10^{-4} RIU	[131]
SiN	Horizontal slot microdisk	15 μm diameter 40 nm slot	7000	Streptavidin 2.5 μg/ml	[132]
Silica	Microtoroid	30 nm diameter	$\sim 10^8$	30-nm radius nanoparticles	[133]
SiN	Hurricane	20 μm diameter	20 000	3 nanoparticles 100 nm size	[134]

13.1. Microring-based biosensors

Microring resonators have been most commonly adopted as biosensors due to the simple cavity shape and single-mode resonances [127]. One important concern for microring resonator-based biosensors is how to quantitatively control and calibrate the resonances of a sensing device. The inevitable fabrication errors or environmental variations limit the sensitivity and the reliability.

In order to improve the reliability, an array of SOI microring resonators was proposed in which some microring resonators serve as references and some microring resonators serve as sensors [128], as shown in Fig. 34a, for robust and label-free detection of a clinically important (carcinoembryonic antigen (CEA)) protein biomarker in undiluted serum. Based on the initial-slope-based quantization method (Fig. 34b), the CEA concentrations at clinically relevant levels (5–100 ng/ml) were measured, which is comparable to a commercial enzyme-linked immunosorbent assay (ELISA) kit.

The sensitivity of the microresonator-based biosensor can be improved by increasing the optical interaction length [129]. Their designed folded structure of a microring resonator has a length of 1.2 mm in a 150 μm × 150 μm sensing area. By extending the ring waveguide length, they demonstrated enhancement of the Q factor, sensitivity and detection limit of the microring sensor.

13.2. Slot microresonator-based biosensors

Integrating slot structures to microresonators has been proposed as another approach to improve the sensitivity. Both the enlarged surface area and the strong field confinement in the slot enhance the interaction between the evanescent field

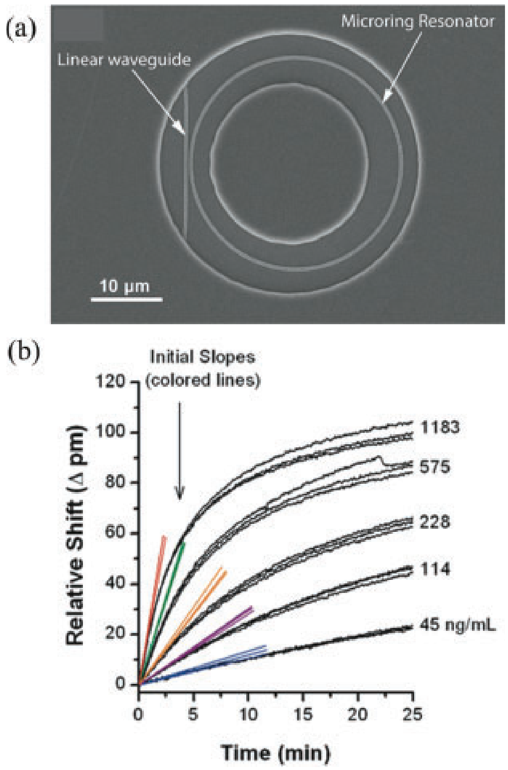

Figure 34 (online color at: www.lpr-journal.org) Top-view SEM of a waveguide-coupled microring resonator with a sensing window in the upper cladding layer. (b) Measured resonance wavelength shifts as a function of time upon various concentrations of CEA. At each concentration, three measured curves are shown for the same ring. The colored traces are tangent to the black curves at $t = 0$ min, and are used to determine the initial slopes of the sensor response. Reproduced with permission from [128], ©2009 ACS.

and the sensing material. A slot-waveguide-based SOI microring resonator has been demonstrated as a biosensor with enhanced sensitivity compared with a normal waveguide microring resonator [130]. The functionalized 100-nm wide slot waveguide showed an increased sensitivity with a factor of 3.5 for protein detection. However, the propagation loss in a slot waveguide can be quite large (12 dB/cm), resulting in a relatively low Q factor of 330 and limited detection.

All the above silicon-based microresonator biosensors were demonstrated on the SOI platform that has some key merits including high refractive-index contrast, easy to be functionalized and low propagation loss. However, the working wavelength is typically limited to the 1550-nm telecommunications range, which is arguably not suitable for biomedical applications due to the strong water absorption near 1550 nm and the resulting thermal and thermophoresis issues [135]. Besides, the telecommunications wavelengths are not detectable by standard silicon CCD cameras.

As an alternative silicon-based platform, SiN is essentially transparent to visible and near-IR light. A slot waveguide microring sensor has been demonstrated on a Si_3N_4-SiO_2 platform [131]. The drawback of such slot microresonators, however, is the difficult fabrication of submicrometer-sized vertical slots. In this regard, e-beam lithography or DUV photolithography are needed in order to accurately control the slot width.

In order to address the fabrication challenge of vertical slots, a SiN microdisk with a 40-nm wide horizontal air slot was demonstrated for biosensing applications [132]. With multilayer deposition and selective etching, ultrathin slots with extremely smooth slot walls were fabricated by means of micrometer-resolution photolithography. Figure 35a shows the SEM picture of the fabricated microdisk with an air slot [132]. The demonstrated Q factor was around 7000. The sensitivity of surface-binding streptavidin was 2.5 ± 0.2 nm/(mg/ml), as shown in Fig. 35b.

13.3. Nanoparticle detection

While most microresonator-based biosensors demonstrated to date focus on biomaterial concentration sensing, there are some studies that have demonstrated single molecule or nanoparticle detection. When a nanoparticle is attached to the microresonator surface, the particle scatters the cavity traveling-wave modes to their opposite directions. Such nanoparticle-induced scattering results in coupling between CW and CCW propagating modes, and thus induces mode splitting in ultrahigh Q microresonators. The ratio of the modes splitting to the scattering loss induced resonance width modification is related to the nanoparticle size. Based on such a mode-splitting-based nanoparticle sensing principle, nanoparticle detection and sizing were demonstrated in an ultrahigh Q microresonator [133].

Novel-shaped microresonators were also used for metal nanoparticle sensing [134]. The SiN microdisk resonator of the hurricane shape generally has low transmission intensity as the cavity traveling-wave direction is normally opposite to the output port, as shown in Fig. 36a. The nanoparticles attached on the microdisk surface can scatter the cavity mode into a counterpropagating direction, thus enhancing the transmission intensity (Fig. 36b). By detecting the intensity rise, one can sense the particle-binding events. The detection limit demonstrated in the experiment is 3 nanoparticles (100 nm diameter). Figure 36c shows the SEM of the device attached with metal nanoparticles.

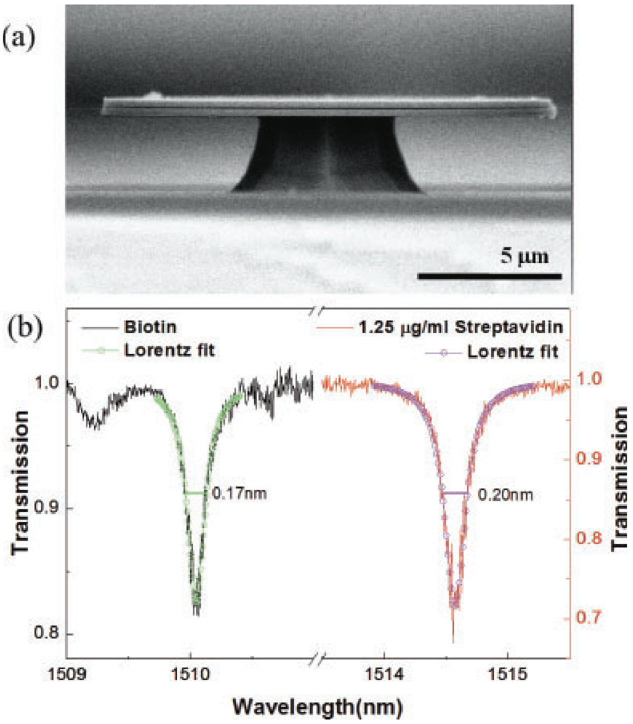

Figure 35 (online color at: www.lpr-journal.org) A SiN microdisk resonator-based biosensor with a horizontal slot. (a) SEM of the fabricated device. (b) Measured transmission spectra before (black) and after (red) binding of streptavidin. Lorentzian fits for before binding (green) and after binding (pink). Reproduced with permission from [132], ©2010 OSA.

14. Microparticle manipulation in optofluidic chips

In this section, we discuss a recent biosensing research direction regarding the use of silicon-based microresonators for on-chip optical manipulation of microparticles. This is a natural extension of the optical manipulation of microparticles using waveguides integrated with microfluidic channels [136–138]. Microresonators with the ability of routing light and storing strong cavity fields can in principle expand the functionalities of waveguide-based micro/nanoparticles routing and storing in an optofluidic circuit [139–142].

Previously, Yang et al [141] demonstrated the use of an on-resonance cavity-enhanced field in a SU-8 microring resonator for propelling a microparticle with a velocity 4–5 times that of a microparticle driven by a SU-8 waveguide. They also demonstrated that by tuning the wavelength

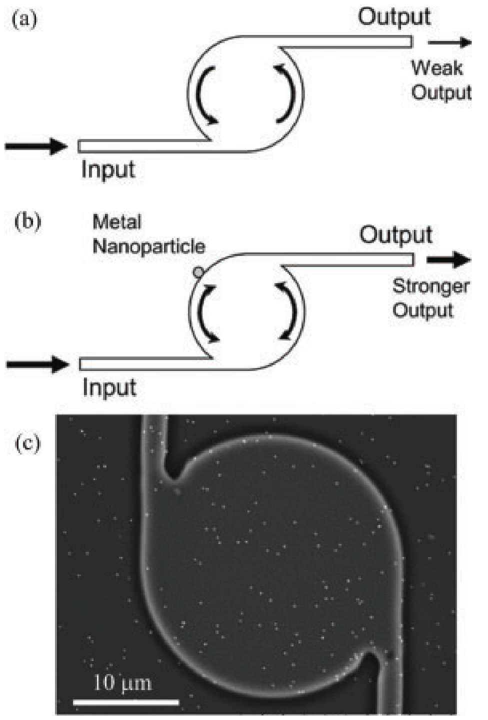

Figure 36 (online color at: www.lpr-journal.org) Schematic of the hurricane-shaped microdisk resonator (a) without and (b) with a metal nanoparticle coupled to the microdisk. The particle scattering induces a stronger output intensity. (c) SEM of the device attached with metal nanoparticles. Reproduced from [134]. ©2010 Elsevier.

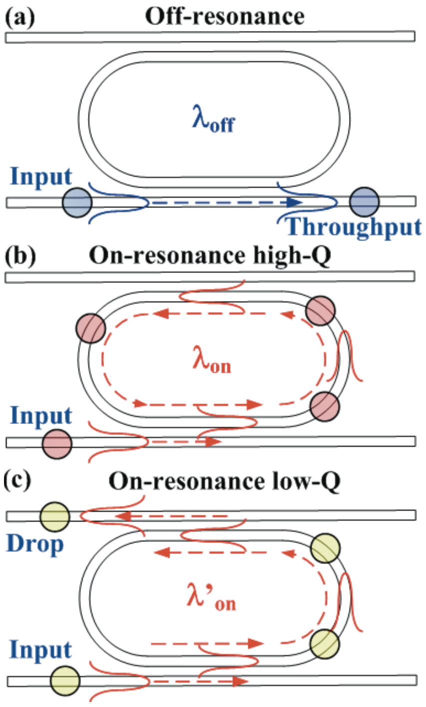

Figure 37 (online color at: www.lpr-journal.org) (a–c) Schematic of optical manipulation of microparticles on a microring-resonator-based add-drop device: (a) Microparticle throughput at an off-resonance wavelength λ_{off}; (b) microparticle buffering at a high-Q resonance wavelength λ_{on}; (c) microparticle dropping at a low-Q resonance wavelength λ'_{on}.

between off- and on-resonance, microparticles could be manipulated to pass through the coupled bus waveguide, or be trapped by the microring waveguide.

Silicon waveguides have a higher refractive index compared to SU-8 based waveguides. The high index contrast leads to cavities with higher-Q resonance modes, and thus evanescent fields with a larger amplitude and gradient. Lin et al [142] demonstrated the optical manipulation of microparticles on a SOI microring coupled with a single waveguide configured as an optical notch filter. The guided power threshold for trapping a microparticle in a microresonator was only ~ 0.67 mW, which was almost one order of magnitude lower than that in the bus waveguide. For a microresonator with Q factor of ~ 1515, the optical potential over the entire microring circumference reached a depth of $25k_BT$ when the microring resonator was on resonance (where k_BT is the room-temperature thermal energy). The microparticles traveled around the microring of radius 5 or 10 µm at hundreds of micrometers per second, producing periodic revolutions at a few hertz.

Previously, we proposed and realized a microparticle add-drop device by using a SiN microring resonator-based add-drop filter in TM polarization [139]. We chose the SiN platform because of its wide transparent window spanning the visible and near-infrared wavelengths and sufficiently large refractive-index contrast with water medium. The TM-mode is preferred for waveguide-based optical manipulation as it has a stronger evanescent field on the waveguide top surface as compared to the TE-mode. We have demonstrated microparticles being transported to the throughput port, trapped in round trips on the microring resonator or routed to the drop port by selecting the carrier wavelength and the resonance Q factor [139].

Figure 37 schematically illustrates the mechanism of optical manipulation of microparticles on a traveling-wave microring resonator-based add-drop device. Microparticles that are located in close proximity to the waveguide and spatially overlap with the waveguide evanescent wave can be vertically trapped by the gradient force and longitudinally driven by the scattering force. At the microring off-resonant wavelengths (λ_{off}), optically driven microparticles remain transported to the throughput port, as shown in Fig. 37a. At the microring on-resonant wavelengths (λ_{on}), the guided field in the throughput waveguide is destructively interfered while that in the microring and the drop waveguide is constructively interfered. Thus, the on-resonant microring can route the microparticles from the input waveguide to the microring. For sufficiently enhanced microring field (namely larger than the drop-waveguide field), the microparticles can be trapped in round-trips, as shown in Fig. 37b. While for relatively less enhanced microring field at a low-Q resonance wavelength λ'_{on} (namely comparable to the drop-waveguide field), the microparticles can be output-coupled to the drop waveguide, as shown in Fig. 37c.

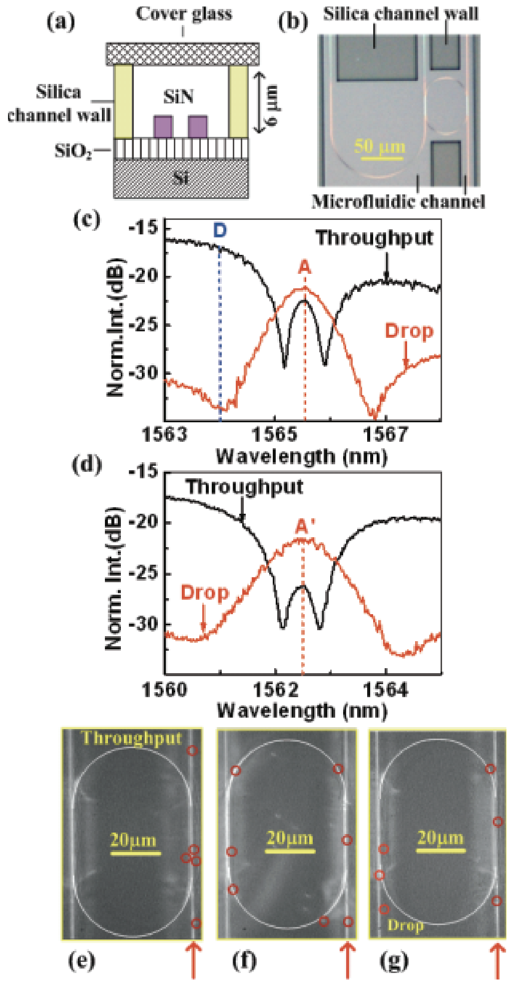

Figure 38 (online color at: www.lpr-journal.org) (a) Schematic cross-sectional view of the optofluidic device. (b) Optical micrograph of the microring racetrack resonator-based add-drop device and the microfluidic channel. (c) Measured throughput- and drop-port transmission spectra of the device with Q ∼ 1506. (d) Measured throughput- and drop-port transmission spectra of the device with Q ∼ 1149. (e)–(g) Optical micrographs of the device with microparticle positions (indicated by the red circles) at various times upon illumination at (e) off-resonance wavelength D, (f) on-resonance wavelength A and (g) on-resonance wavelength A'. Reproduced with permission from [139], ©2010 OSA.

Figure 38a shows a schematic cross section of the integrated optofluidic device [139]. For the fluidic layer, we adopted the photolithographic method to pattern the silica channel in order to lithographically align the microfluidic layer to the photonic layer. The silica-based microfluidic channels were 6 μm in height and covered with a cover glass. Figure 38b shows an optical micrograph of the optofluidic device [139].

Figure 38c shows the measured throughput- and drop-port transmission spectra of the microring add-drop device [139]. The resonance *Q* factor was ∼ 1506 according to the drop-port spectrum. When we tuned the input laser wavelength to an off-resonance wavelength D (1564 nm), microparticles were transported to the throughput port, as shown in Fig. 38e [139].

Figure 38f shows that at on-resonance wavelength A (1565.56 nm), a microparticle was routed from the input waveguide to the microring and guided for at least one round trip in the microring resonator [139]. This suggests that the microresonator field intensity was sufficiently higher than that in the input- and drop waveguides.

Figure 38d shows the measured throughput- and drop-port transmission spectra of another microring add-drop device of identical design [139]. The *Q* factor was ∼ 1149 according to the drop-port spectrum. Figure 38g shows that at on-resonance wavelength A' (1562.5 nm), a microparticle was transported from the input waveguide via the microring to the drop port [139]. This suggests that the microring field intensity was comparable to that in the drop waveguide.

The various functions of trapping and routing microparticles using silicon-based microresonators can constitute building blocks of the future "microparticle circuits" for lab-on-a-chip applications, as visualized in Fig. 2.

15. Summary, challenges and outlook

In summary, we have reviewed extensively the fundamentals, various applications, issues and state-of-the-art of silicon microresonators. In particular, we have discussed in detail about total-internal-reflection-based microring and microdisk resonators in various shapes including circular, racetrack, polygonal, microspiral and double-notch-shaped, and various structures spanning single-element, cascaded and interferometer-coupled microresonators. We have reviewed silicon-based microresonators integrated with microelectronic devices, microheaters, liquid crystals and microfluidics. Such silicon microresonators have shown unique functionalities and potential applications as filters, modulators, switches, routers, delay lines, detectors and optical signal processing components for on-chip optical interconnections, and also as biosensors and particle manipulation devices for lab-on-a-chip applications. In addition, we have highlighted some of the known issues such as silicon microresonator losses, light coupling to microresonators, narrowband resonances that are limiting high-speed data transmissions, and power consumption and speed of tuning and switching silicon microresonators.

However, in order to realize practical on-chip applications of silicon-based microresonators and silicon photonics in general, many mid- to long-term scientific and engineering challenges still remain to be addressed. Here, we outline seven challenges spanning from analytical modeling to integration as follows:

1. Advanced analytical modeling tools that can complement existing theoretical modeling methods such as transfer matrix modeling and coupled-mode theory to provide quantitative analysis from the first principle regarding, for instance, silicon microresonator losses, light coupling to silicon microresonators including intercavity coupling, resonance mode distributions of a single device as well as across a highly coupled structure, statistical variations

of the microresonator morphologies and of the coupled waveguide and ring waveguide dimensions should help better model the fabricated device performance.

2. Design rules and verification procedures to streamline the design of silicon microresonator-based devices and circuits, particularly for complex photonic devices and large-scale-integrated circuits with advanced functionalities.
3. Foundry CMOS fabrication of silicon-based microresonators and silicon photonics in general to satisfy the tight fabrication constraint for reliable batch processes. Ultimately, the CMOS electronic and photonic fabrication processes should be fully integrated.
4. Effective heat-management methods have been relatively less addressed in the silicon microresonator literature, yet heat management is absolutely crucial in order to enable effective stabilization of microresonator resonance wavelengths and lineshapes. For telecommunications applications, we should devise ways to thermally stabilize silicon-based microresonators within a relatively large temperature range of -40 to $+80$ °C. For on-chip optical interconnections, with large-scale integration expected and possibly on-chip laser sources and other heat-dissipating components, the thermal control could be even more demanding.
5. High optical power handling issue involves optical, electrical and thermal management, and it is relatively less addressed in the silicon photonics literature. High optical power results in nonlinear two-photon absorption, which generates heat and free carriers (See Sect. 3). The generated heat results in resonance wavelength redshifts. The generated free carriers result in resonance wavelength blueshifts by free-carrier dispersion and optical loss by free-carrier absorption. In particular, microresonator-based optical modulator performances can be strongly affected by the resonance wavelength shifts and lineshape change upon high optical power (see Sect. 7).
6. Effective polarization management method is another relatively less addressed issue in the silicon microresonator literature. Silicon submicrometer-sized waveguides are highly polarization sensitive and usually only propagate TE polarization modes. Moreover, silicon microresonators typically support nondegenerate TE and TM modes. Thus, in order to enable telecommunications applications with optical fiber coupling randomly polarized signals to the chip, we must devise either polarization management schemes (such as polarization splitters/combiners and rotators) to couple TE/TM light with different microresonators or polarization-insensitive microresonators at particular wavelength channels.
7. Integration with CMOS nanoelectronics to enable intelligent, reconfigurable, high-speed, low-voltage, low-power-consumption and compact-footprint on-chip optical interconnects with vertically integrated active electrical control of silicon or hybrid silicon microresonators. Such integration will likely be implemented on a multilayer architecture with the silicon-based or hybrid silicon photonic layer on top of the CMOS electronic layer.

We also expect to see many new developments from nascent areas using silicon-based microresonators. Here, we highlight three of them that we feel are particularly promising as follows:

15.1. Hybrid silicon unidirectional microresonator-based lasers

Microresonator-based lasers demonstrated in hybrid silicon platform nowadays are emitting light in two directions as the microresonators support degenerately CW and CCW lasing modes. Half of the lasing power is inevitably lost when only a single output is utilized. Current solutions to address this issue include 1) external methods to break the CW-CCW symmetry, such as seeding the lasing in a preferred direction [143] or employing an external feedback on one of the two output directions [144], and 2) CW-CCW mode symmetry breaking due to the nonlinear effect under high-pumping conditions [145, 146].

An alternative approach is to employ a microresonator structure that inherently breaks the symmetry between CW and CCW lasing modes. One of these potential microresonator structures is the spiral-shaped microdisk resonator reviewed in this article in Sect. 5. In fact, the unidirectional laser emission from such microspiral lasers has long been realized in III-V semiconductors and dye-doped polymer platforms [52, 147]. When applying such microspiral disk resonators to hybrid III-V integrated silicon platform as a unidirectional microlaser cavity, the main issues of concern will be to enable power-efficient electrically pumped laser light to unidirectionally couple to an integrated silicon waveguide.

15.2. Deposited thin-film-based microresonators on silicon substrates

Although microresonator-based devices on SOI platform have seen significant developments over the past decade, we believe the SOI platform may not be the final solution to on-chip photonic integrated circuits. On the front of optical interconnects applications, the current CMOS microelectronics architecture has multiple metal interconnect layers, and thus it is arguably more feasible to have the photonic layer integrated on the top of the electrical layers. As such, we believe microresonator-based devices fabricated on deposited thin films, such as SiN [148], SiON [149] and polysilicon [116] could find significant applications to this end. On the front of the optical biosensing and optofluidics, light sources in the visible and near-infrared range other than the telecommunications wavelengths are preferred in order to avoid strong optical absorption in water. Thus, we believe microresonators on a SiN thin-film platform that is transparent to visible and near-infrared wavelengths has potential in such areas.

15.3. Integrated silicon-based microresonators for lab-on-a-chip applications

In order to realize practical lab-on-a-chip applications using silicon-based microresonators, significant efforts should be devoted to enabling microresonator-based sensors with reliable high sensitivity and ease of calibration or referencing (for clinical diagnostic or laboratory-level testing), portability and high throughputs. We also expect to see more optical manipulation functionalities becoming possible using silicon-based microresonator circuits integrated with micro-/nanofluidics to enable micro/nanoparticles of various biological natures to be selectively transported, buffered, dropped and sorted with possibly high throughput.

Acknowledgements. The authors would like to acknowledge financial support by grants from the Research Grants Council of The Hong Kong Special Administrative Region, China, under projects no. 618505, 618506, 618707, 618308 and 618010. The authors gratefully acknowledge the HKUST Nanoelectronics Fabrication Facility for the silicon chip nanofabrication for various work reviewed in this article. We also acknowledge fruitful discussions with Yu Zhang and Aimé Sayarath.

Received: 22 March 2011, **Revised:** 19 May 2011, **Accepted:** 17 June 2011

Key words: Silicon photonics, microresonators, on-chip optical interconnects, biosensors, microparticle manipulation, filters, modulators, delay lines.

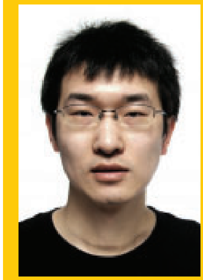

Shaoqi Feng received his B. E. degree of Optoelectronics from Nankai University, Tianjin, China, in 2008. He is now studying for the Ph. D. degree in the Department of Electronic and Computer Engineering, The Hong Kong University of Science and Technology, Hong Kong. His research interests include silicon photonics and optical microresonators for telecommunications and on-chip optical interconnects.

Ting Lei received the B. S. and M. S. degrees in Optics from Nankai University, Tianjin, China, in 2006 and 2009, respectively. He is now working towards a Ph. D. degree in the Department of Electronic and Computer Engineering, The Hong Kong University of Science and Technology, Hong Kong. His research interestings focus on cascaded microresonators structure and on chip biosensing. He is a student member of IEEE.

Hui Chen received his B. E. degree in telecommunication engineering from Beijing University of Posts and Telecommunications, Beijing, China, in 2000. He received his M. Phil. and Ph. D. degree in electrical and electronic engineering from The Hong Kong University of Science and Technology, Hong Kong, in 2003 and 2010, respectively.

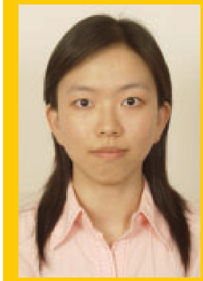

Hong Cai received her B. E. degree of Optoelectronic from South China Normal University, Guangzhou, Guangdong, China, in 2005 and M. S. degree of Optical Engineering, in Shanghai Institute of Optics and Fine Mechanics, Chinese Academy of Science, Shanghai, China, in 2008. She is currently studying for the Ph. D. degree in the Department of Electronic and Computer Engineering in The Hong Kong University of Science and Technology, Hong Kong. Her research interest is in optical manipulation of micro/nano particles on optofluidic chips techniques and applications.

Xianshu Luo received his B. E. degree of Microelectronics from Jilin University, Changchun, Jilin, China, in 2003 and his M. S. degree of microelectronics and solid state physics from Institute of Semiconductors, Chinese Academy of Science, Beijing, China, in 2006. He received his Ph. D. degree in electrical and electronic engineering from The Hong Kong University of Science and Technology, Hong Kong, in 2010. He is now a senior research engineer in Insitute of Microelectronics, A*STAR, Singapore.

Andrew Wing On Poon received his Ph. D. and M. Phil. degrees in physics from Yale University, New Haven, in 2001 and 1998, respectively. He received his B. A. degree (with honors) in physics from The University of Chicago, Illinois, in 1995. In 2001 he joined the department of electronic and computer engineering, The Hong Kong University of Science and Technology (HKUST), as an assistant professor. He is now an associate professor. He has authored or co-authored more than 100 papers in journals and international conferences, co-authored two book chapters, co-edited one book, and awarded one patent. He has served as the chair of The IEEE Photonics Society Hong Kong Chapter (2008-2009). During his 2nd term tenure, the Hong Kong Chapter was awarded the Society "Chapter of the Year" Award 2009. He has served on various technical program committees of international conferences. He is currently an Associate Editor of IEEE Photonics Technology Letters. His research interests include silicon photonics and optical microresonators for telecommunications, on-chip optical interconnects and biosensing.

References

[1] R. K. Chang and A. J. Campillo, Optical Processes in Microcavities (World Scientific, Singapore, 1996).
[2] K. J. Vahala, Optical Microcavities (World Scientific, Singapore, 2004).
[3] A. B. Matsko, Practical Applications of Microresonators in Optics and Photonics (CRC Press, Boca Raton, 2009).
[4] A. Serpengüzel and A. W. Poon, Optical Processes in Microparticles and Nanostructures (World Scientific, Singapore, 2011).
[5] K. J. Vahala, Nature **424**, 839–846 (2003).
[6] A. B. Matsko and V. S. Ilchenko, IEEE J. Sel. Top. Quantum Electron. **12**, 3–14 (2006).
[7] V. S. Ilchenko and A. B. Matsko, IEEE J. Sel. Top. Quantum Electron. **12**, 15–32 (2006).
[8] E. A. J. Marcatilli, Bell Syst. Tech. J. **48**, 2103–2132 (1969).
[9] B. E. Little, J. S. Foresi, G. Steinmeyer, E. R. Thoen, S. T. Chu, H. A. Haus, E. P. Ippen, L. C. Kimerling, and W. Greene, IEEE Photon. Technol. Lett. **10**, 549–551 (1998).
[10] M. L. Gorodetsky, A. A. Savchenkov, and V. S. Ilchenko, Opt. Lett. **21**, 453–455 (1996).
[11] D. Rafizadeh, J. P. Zhang, S. C. Hagness, A. Taflove, K. A. Stair, S. T. Ho, and R. C. Tiberio, Opt. Lett. **22**, 1244–1246 (1997).
[12] P. Rabiei, W. H. Steier, C. Zhang, and L. R. Dalton, J. Lightwave Technol. **20**, 1968–1975 (2002).
[13] S. Suzuki, K. Shuto, and Y. Hibino, IEEE Photon. Technol. Lett. **4**, 1256–1258 (1992).
[14] F. Xia, L. Sekaric, and Y. Vlasov, Nature Photon. **1**, 65–71 (2007).
[15] D. Liang and J. E. Bowers, Nature Photon. **4**, 511–517 (2010).
[16] J. Leuthold, C. Koos, and W. Freude, Nature Photon. **4**, 535–544 (2010).
[17] N. Daldosso and L. Pavesi, Laser Photon. Rev. **3**, 508–534 (2009).
[18] N. Q. Vinh, N. N. Ha, and T. Gregorkiewicz, Proc. IEEE **97**, 1269–1283 (2009).
[19] L. Tsybeskov and D. J. Lockwood, Proc. IEEE **97**, 1284–1303 (2009).
[20] C. Batten, A. Joshi, J. Orcutt, A. Khilo, B. Moss, C. W. Holzwarth, M. A. Popovic, H. Q. Li, H. I. Smith, J. L. Hoyt, F. X. Kartner, R. J. Ram, V. Stojanovic, and K. Asanovic, IEEE Micro **29**, 8–21 (2009).
[21] D. Van Thourhout, T. Spuesens, S. K. Selvaraja, L. Liu, G. Roelkens, R. Kumar, G. Morthier, P. Rojo-Romeo, F. Mandorlo, P. Regreny, O. Raz, C. Kopp, and L. Grenouillet, IEEE J. Sel. Top. Quantum Electron. **16**, 1363–1375 (2010).
[22] S. Assefa, F. N. Xia, W. M. J. Green, C. L. Schow, A. V. Rylyakov, and Y. A. Vlasov, IEEE J. Sel. Top. Quantum Electron. **16**, 1376–1385 (2010).
[23] L. Stampoulidis, K. Vyrsokinos, K. Voigt, L. Zimmermann, F. Gomez-Agis, H. J. S. Dorren, Z. Sheng, D. Van Thourhout, L. Moerl, J. Kreissl, B. Sedighi, J. C. Scheytt, A. Pagano, and E. Riccardi, IEEE J. Sel. Top. Quantum Electron. **16**, 1422–1433 (2010).
[24] T. J. Kippenberg and K. J. Vahala, Science **321**, 1172–1176 (2008).
[25] T. Baba, Nature Photon. **2**, 465–473 (2008).
[26] L. Pavesi and D. J. Lockwood, Silicon Photonics (Springer-Verlag, Berlin, 2004).
[27] G. T. Reed and A. P. Knights, Silicon Photonics: an Introduction (Wiley, Chichester, 2004).
[28] G. Reed, Silicon Photonics: the State of the Art (Wiley, Chichester, 2008).
[29] B. Jalali and S. Fathpour, Silicon Photonics for Telecommunications & Biomedical Applications (CRC Press, Boca Raton, 2010).
[30] L. Pavesi and G. Guillot, Optical Interconnects: the Silicon Approach (Springer-Verlag, Berlin, 2006).
[31] D. Miller, Proc. IEEE **97**, 1166–1185 (2009).
[32] K. Ohashi, K. Nishi, T. Shimizu, M. Nakada, J. Fujikata, J. Ushida, S. Torii, K. Nose, M. Mizuno, and H. Yukawa, Proc. IEEE **97**, 1186–1198 (2009).
[33] F. B. Myers and L. P. Lee, Lab Chip **8**, 2015–2031 (2008).
[34] N. Jokerst, M. Royal, S. Palit, L. Luan, S. Dhar, and T. Tyler, J. Biophoton. **2**, 212–226 (2009).
[35] A. Yariv, Electron. Lett. **36**, 321–322 (2000).
[36] M. Soltani, S. Yegnanarayanan, Q. Li, and A. Adibi, IEEE J. Quantum Electron. **46**, 1158–1169 (2010).
[37] D. K. Sparacin, S. J. Spector, and L. C. Kimerling, J. Lightwave Technol. **23**, 2455–2461 (2005).
[38] R. Jones, J. Doylend, P. Ebrahimi, S. Ayotte, O. Raday, and O. Cohen, Opt. Express **15**, 15836–15841 (2007).
[39] H. S. Rong, S. B. Xu, Y. H. Kuo, V. Sih, O. Cohen, O. Raday, and M. Paniccia, Nature Photon. **1**, 232–237 (2007).
[40] M. Borselli, T. J. Johnson, and O. Painter, Opt. Express **13**, 1515–1530 (2005).
[41] M. Borselli, T. Johnson, and O. Painter, Appl. Phys. Lett. **88**, 131114 (2006).
[42] M. Borselli, T. J. Johnson, C. P. Michael, M. D. Henry, and O. Painter, Appl. Phys. Lett. **91**, 131117 (2007).
[43] M. Borselli, T. J. Johnson, and O. Painter, Opt. Lett. **32**, 2954–2956 (2007).
[44] K. K. Tsia, S. Fathpour, and B. Jalali, Opt. Express **14**, 12327–12333 (2006).
[45] S. Fathpour, K. K. Tsia, and B. Jalali, IEEE J. Sel. Top. Quantum Electron. **43**, 1211–1217 (2007).
[46] H. Chen and A. W. Poon, Appl. Phys. Lett. **96**, 191106 (2010).
[47] H. A. Haus, Waves and Fields in Optoelectronics (Prentice-Hall, New Jersey, 1984).
[48] Q. Xu, D. Fattal, and R. Beausoleil, Opt. Express **16**, 4309–4315 (2008).
[49] D. X. Xu, A. Densmore, P. Waldron, J. Lapointe, E. Post, A. Delage, S. Janz, P. Cheben, J. H. Schmid, and B. Lamontagne, Opt. Express **15**, 3149–3155 (2007).
[50] A. W. Poon, X. Luo, L. Zhou, C. Li, J. Y. Lee, F. Xu, H. Chen, and N. K. Hon, Microresonator-based devices on a silicon chip: Novel shaped cavities and resonance coherent interference, in: Practical Applications of Microresonators in Optics and Photonics, edited by A. B. Matsko (CRC Press, Boca Raton, 2009).
[51] C. Li, L. J. Zhou, S. M. Zheng, and A. W. Poon, IEEE J. Sel. Top. Quantum Electron. **12**, 1438–1449 (2006).
[52] G. D. Chern, H. E. Tureci, A. D. Stone, R. K. Chang, M. Kneissl, and N. M. Johnson, Appl. Phys. Lett. **83**, 1710–1712 (2003).
[53] J. Y. Lee, X. S. Luo, and A. W. Poon, Opt. Express **15**, 14650–14666 (2007).
[54] X. Luo and A. W. Poon, Chin. Opt. Lett. **7**, 296–298 (2009).

[55] S. J. Xiao, M. H. Khan, H. Shen, and M. H. Qi, J. Lightwave Technol. **26**, 228–236 (2008).

[56] R. Boeck, N. A. F. Jaeger, N. Rouger, and L. Chrostowski, Opt. Express **18**, 25151–25157 (2010).

[57] T. Barwicz, M. A. Popovic, P. T. Rakich, M. R. Watts, H. A. Haus, E. P. Ippen, and H. I. Smith, Opt. Express **12**, 1437–1442 (2004).

[58] S. Xiao, M. H. Khan, H. Shen, and M. H. Qi, Opt. Express **15**, 14765–14771 (2007).

[59] F. Xia, L. Sekaric, M. O'Boyle, and Y. Vlasov, Appl. Phys. Lett. **89**, 041122 (2006).

[60] F. N. Xia, M. Rooks, L. Sekaric, and Y. Vlasov, Opt. Express **15**, 11934–11941 (2007).

[61] Q. Li, M. Soltani, S. Yegnanarayanan, and A. Adibi, Opt. Express **17**, 2247–2254 (2009).

[62] G. T. Reed, G. Mashanovich, F. Y. Gardes, and D. J. Thomson, Nature Photon. **4**, 518–526 (2010).

[63] R. Soref and B. Bennett, IEEE J. Quantum Electron. **23**, 123–129 (1987).

[64] S. Manipatruni, L. Chen, and M. Lipson, Opt. Express **18**, 16858–16867 (2010).

[65] Q. Xu, B. Schmidt, S. Pradhan, and M. Lipson, Nature **435**, 325–327 (2005).

[66] S. Manipatruni, Q. Xu, B. S. Schmidt, J. Shakya, and M. Lipson, in IEEE LEOS 2007 (IEEE, 2007), paper WO2.

[67] L. Zhou and A. W. Poon, Opt. Express **14**, 6851–6857 (2006).

[68] P. Dong, S. Liao, H. Liang, W. Qian, X. Wang, R. Shafiiha, D. Feng, G. Li, X. Zheng, A. V. Krishnamoorthy, and M. Asghari, Opt. Lett. **35**, 3246–3248 (2010).

[69] X. Zheng, J. Lexau, Y. Luo, H. Thacker, T. Pinguet, A. Mekis, G. Li, J. Shi, P. Amberg, N. Pinckney, K. Raj, R. Ho, J. E. Cunningham, and A. V. Krishnamoorthy, Opt. Express **18**, 3059–3070 (2010).

[70] F. Y. Gardes, A. Brimont, P. Sanchis, G. Rasigade, D. Marris-Morini, L. O'Faolain, F. Dong, J. M. Fedeli, P. Dumon, L. Vivien, T. F. Krauss, G. T. Reed, and J. Marti, Opt. Express **17**, 21986–21991 (2009).

[71] P. Dong, S. Liao, D. Feng, H. Liang, D. Zheng, R. Shafiiha, C. Kung, W. Qian, G. Li, X. Zheng, A. V. Krishnamoorthy, and M. Asghari, Opt. Express **17**, 22484–22490 (2009).

[72] C. Gunn, IEEE Micro **26**, 58–66 (2006).

[73] J. B. You, M. Park, J. W. Park, and G. Kim, Opt. Express **16**, 18340–18344 (2008).

[74] J.C. Rosenberg, W. M. J. Green, S. Assefa, T. Barwicz, M. Yang, S. M. Shank, and Y. Vlasov, in: Proceedings of the Conference on Laser and Electro-Optics 2011 (Optical Society of America, 2011), paper PDPB9.

[75] M. R. Watts, D. C. Trotter, R. W. Young, and A. L. Lentine, Ultralow power silicon microdisk modulators and switches, in: Proceedings of the 2008 5th IEEE International Conference on Group IV Photonics (IEEE, 2008), paper WA2.

[76] W. A. Zortman, M. R. Watts, D. C. Trotter, R. W. Young, and A. L. Lentine, Low-power high-speed silicon microdisk modulators, in: Proceedings of the Conference on Lasers and Electro-Optics 2010 (Optical Society of America, 2010), paper CThJ4.

[77] A. W. Poon, X. Luo, F. Xu, and H. Chen, Proc. IEEE **97**, 1216–1238 (2009).

[78] F. Xu and A. W. Poon, Opt. Express **16**, 8649–8657 (2008).

[79] H. Chen and A. W. Poon, IEEE Photon. Technol. Lett. **18**, 2260–2262 (2006).

[80] V. G. Chigrinov, L. Zhou, A. A. Muravsky, and A. W. Poon, Electrically tunable microresonators using photoaligned liquid crystals, US Patent 2007/0258677 A1 (2007).

[81] B. Maune, R. Lawson, C. Gunn, A. Scherer, and L. Dalton, Appl. Phys. Lett. **83**, 4689–4691 (2003).

[82] W. De Cort, J. Beeckman, R. James, F. A. Fernandez, R. Baets, and K. Neyts, Opt. Lett. **34**, 2054–2056 (2009).

[83] F. Gan, T. Barwicz, M. Popovi, M. Dahlem, C. Holzwarth, P. Rakich, H. Smith, E. Ippen, and F. Kärtner, Maximizing the thermo-optic tuning range of silicon photonic structures, in: Proceedings of the IEEE Conference on Photonics in Switching (IEEE, 2007), paper TuB3.3.

[84] P. Dong, W. Qian, H. Liang, R. Shafiiha, N. N. Feng, D. Feng, X. Zheng, A. V. Krishnamoorthy, and M. Asghari, Opt. Express **18**, 9852–9858 (2010).

[85] P. Dong, W. Qian, H. Liang, R. Shafiiha, D. Feng, G. Li, J. E. Cunningham, A. V. Krishnamoorthy, and M. Asghari, Opt. Express **18**, 20298–20304 (2010).

[86] N. Sherwood-Droz, H. Wang, L. Chen, B. G. Lee, A. Biberman, K. Bergman, and M. Lipson, Opt. Express **16**, 15915–15922 (2008).

[87] A. H. Atabaki, E. S. Hosseini, A. A. Eftekhar, S. Yegnanarayanan, and A. Adibi, Opt. Express **18**, 18312–18323 (2010).

[88] M. R. Watts, W. A. Zortman, D. C. Trotter, G. N. Nielson, D. L. Luck, and R. W. Young, Adiabatic Resonant Microrings (ARMs) with directly integrated thermal microphotonics, in: Proceedings of the Conference on Lasers and Electro-Optics 2009 (Optical Society of America, 2009), paper CPDB10.

[89] L. Zhou and A. W. Poon, Opt. Lett. **32**, 781–783 (2007).

[90] Q. Xu, J. Shakya, and M. Lipson, Opt. Express **14**, 6463–6468 (2006).

[91] L. Zhou and A. W. Poon, Opt. Express **15**, 9194–9204 (2007).

[92] C. Y. Chao and L. J. Guo, Appl. Phys. Lett. **83**, 1527–1529 (2003).

[93] M. Terrel, M. J. F. Digonnet, and S. Fan, Appl. Opt. **48**, 4874–4879 (2009).

[94] J. Song, Q. Fang, S. H. Tao, M. B. Yu, G. Q. Lo, and D. L. Kwong, Opt. Express **16**, 8359–8365 (2008).

[95] L. Luo, S. Ibrahim, A. Nitkowski, Z. Ding, C. B. Poitras, S. J. B. Yoo, and M. Lipson, Opt. Express **18**, 23079–23087 (2010).

[96] M. S. Rasras, D. M. Gill, S. S. Patel, K. Y. Tu, Y. K. Chen, A. E. White, A. T. S. Pomerene, D. N. Carothers, M. J. Grove, D. K. Sparacin, J. Michel, M. A. Beals, and L. C. Kimerling, J. Lightwave Technol. **25**, 87–92 (2007).

[97] M. A. Popovi, T. Barwicz, F. Gan, M. S. Dahlem, C. W. Holzwarth, P. T. Rakich, H. I. Smith, E. P. Ippen, and F. X. Kärtner, Transparent wavelength switching of resonant filters, in: Proceedings of the Conference on Lasers and Electro-Optics (Optical Society of America, 2007), paper CPDA2.

[98] C. Li, L. J. Zhou, and A. W. Poon, Opt. Express **15**, 5069–5076 (2007).

[99] D. M. Gill, S. S. Patel, M. Rasras, K. Tu, A. E. White, Y. Chen, A. Pomerene, D. Carothers, R. L. Kamocsai, C. M. Hill, and J. Beattie, IEEE J. Sel. Top. Quantum Electron. **16**, 45–52 (2009).

[100] X. S. Luo, H. Chen, and A. W. Poon, Opt. Lett. **35**, 2940–2942 (2010).

[101] Q. Li, F. Liu, Z. Zhang, M. Qiu, and Y. Su, J. Lightwave Technol. **26**, 3744–3751 (2008).
[102] S. Feng, X. Luo, S. Du, and A. W. Poon, Opt. Lett. **36**, 1278–1280 (2011).
[103] T. Wang, F. F. Liu, J. Wang, Y. Tian, Z. Y. Zhang, T. Ye, M. Qiu, and Y. K. Su, J. Lightwave Technol. **27**, 4734–4743 (2009).
[104] J. E. Heebner, R. Boyd, and Q. Park, Phys. Rev. E **65**, 36619 (2002).
[105] J. Heebner and R. Boyd, J. Mod. Opt. **49**, 2629–2636 (2002).
[106] J. Yang, N. Fontaine, Z. Pan, A. Karalar, S. Djordjevic, C. Yang, W. Chen, S. Chu, B. Little, and S. Yoo, IEEE Photon. Technol. Lett **20**, 1030–1032 (2008).
[107] P. Chak and J. Sipe, Opt. Lett. **31**, 2568–2570 (2006).
[108] S. Mookherjea, J. S. Park, S.-H. Yang, and P. R. Bandaru, Nature Photon. **2**, 90–93 (2008).
[109] M. L. Cooper, G. Gupta, M. A. Schneider, W. M. J. Green, S. Assefa, F. Xia, Y. A. Vlasov, and S. Mookherjea, Opt. Express **18**, 26505–26516 (2010).
[110] A. Melloni, F. Morichetti, C. Ferrari, and M. Martinelli, Opt. Lett. **33**, 2389–2391 (2008).
[111] X. Luo and A. W. Poon, Opt. Express **17**, 23617–23628 (2009).
[112] H. Chen, X. Luo, and A. W. Poon, Appl. Phys. Lett. **95**, 171111 (2009).
[113] J. K. Doylend, P. E. Jessop, and A. P. Knights, Opt. Express **18**, 14671–14678 (2010).
[114] M. W. Geis, S. J. Spector, M. E. Grein, R. T. Schulein, J. U. Yoon, D. M. Lennon, S. Deneault, F. Gan, F. X. Kaertner, and T. M. Lyszczarz, IEEE Photon. Tech. Lett. **19**, 152–154 (2007).
[115] M. W. Geis, S. J. Spector, M. E. Grein, R. T. Schulein, J. U. Yoon, D. M. Lennon, C. M. Wynn, S. T. Palmacci, F. Gan, F. X. Kaertner, and T. M. Lyszczarz, Opt. Express **15**, 16886–16895 (2007).
[116] K. Preston, Y. H. D. Lee, M. A. Zhang, and M. Lipson, Opt. Lett. **36**, 52–54 (2011).
[117] T. K. Liang, H. K. Tsang, I. E. Day, J. Drake, A. P. Knights, and M. Asghari, Appl. Phys. Lett. **81**, 1323–1325 (2002).
[118] J. Bravo-Abad, E. P. Ippen, and M. Soljacic, Appl. Phys. Lett. **94**, 241103 (2009).
[119] L. Zhou, H. Chen, and A. W. Poon, J. Lightwave Technol. **26**, 1950–1955 (2008).
[120] L. Zhang, J. Y. Yang, M. Song, Y. Li, B. Zhang, R. G. Beausoleil, and A. E. Willner, Opt. Express **15**, 11564–11569 (2007).
[121] M. H. Khan, H. Shen, Y. Xuan, L. Zhao, S. J. Xiao, D. E. Leaird, A. M. Weiner, and M. H. Qi, Nature Photon. **4**, 117–U130 (2010).
[122] F. Liu, T. Wang, L. Qiang, T. Ye, Z. Zhang, M. Qiu, and Y. Su, Opt. Express **16**, 15880–15886 (2008).
[123] L. Xu, C. Li, H. K. Tsang, and C. W. Chow, Electron. Lett. **45**, 697–698 (2009).
[124] Q. Chang, Q. Li, Z. Zhang, M. Qiu, T. Ye, and Y. Su, IEEE Photon. Technol. Lett. **21**, 60–62 (2009).
[125] M. Pu, L. Liu, W. Xue, Y. Ding, L. H. Frandsen, H. Ou, K. Yvind, and J. M. Hvam, IEEE Photon. Technol. Lett. **22**, 869–871 (2009).
[126] L. Xu, C. Li, C. Wong, and H. Tsang, IEEE Photon. Technol. Lett. **21**, 295–297 (2009).
[127] K. De Vos, J. Girones, S. Popelka, E. Schacht, R. Baets, and P. Bienstman, Biosens. Bioelectron. **24**, 2528–2533 (2009).
[128] A. L. Washburn, L. C. Gunn, and R. C. Bailey, Anal. Chem. **81**, 9499–9506 (2009).
[129] D. X. Xu, A. Densmore, A. Delage, P. Waldron, R. McKinnon, S. Janz, J. Lapointe, G. Lopinski, T. Mischki, E. Post, P. Cheben, and J. H. Schmid, Opt. Express **16**, 15137–15148 (2008).
[130] T. Claes, J. G. Molera, K. De Vos, E. Schacht, R. Baets, and P. Bienstman, IEEE Photon. J. **1**, 197–204 (2009).
[131] C. A. Barrios, K. B. Gylfason, B. Sanchez, A. Griol, H. Sohlstrom, M. Holgado, and R. Casquel, Opt. Lett. **32**, 3080–3082 (2007).
[132] S. Lee, S. C. Eom, J. S. Chang, C. Huh, G. Y. Sung, and J. H. Shin, Opt. Express **18**, 20638–20644 (2010).
[133] J. G. Zhu, S. K. Ozdemir, Y. F. Xiao, L. Li, L. N. He, D. R. Chen, and L. Yang, Nature Photon. **4**, 46–49 (2010).
[134] B. Koch, L. Carson, C. M. Guo, C. Y. Lee, Y. S. Yi, J. Y. Zhang, M. Zin, S. Znameroski, and T. Smith, Sens. Actuators B, Chem. **147**, 573–580 (2010).
[135] F. M. Weinert and D. Braun, J. Appl. Phys. **104**, 104701 (2008).
[136] S. Gaugiran, S. Getin, J. M. Fedeli, G. Colas, A. Fuchs, F. Chatelain, and J. Derouard, Opt. Express **13**, 6956–6963 (2005).
[137] A. H. J. Yang, S. D. Moore, B. S. Schmidt, M. Klug, M. Lipson, and D. Erickson, Nature **457**, 71–75 (2009).
[138] H. Cai and A. W. Poon, Optical manipulation of microbeads in an integrated optofluidic device, in: Proceedings of the Conference on Lasers and Electro-Optics 2010 (Optical Society of America, 2010).
[139] H. Cai and A. W. Poon, Opt. Lett. **35**, 2855–2857 (2010).
[140] S. Mandal, X. Serey, and D. Erickson, Nano Lett. **10**, 99–104 (2010).
[141] A. H. J. Yang and D. Erickson, Lab Chip **10**, 769–774 (2010).
[142] S. Y. Lin, E. Schonbrun, and K. Crozier, Nano Lett. **10**, 2408–2411 (2010).
[143] A. W. Fang, B. R. Koch, K. G. Gan, H. Park, R. Jones, O. Cohen, M. J. Paniccia, D. J. Blumenthal, and J. E. Bowers, Opt. Express **16**, 1393–1398 (2008).
[144] A. W. Fang, R. Jones, H. Park, O. Cohen, O. Raday, M. J. Paniccia, and J. E. Bowers, Opt. Express **15**, 2315–2322 (2007).
[145] J. P. Hohimer and G. A. Vawter, Appl. Phys. Lett. **63**, 2457–2459 (1993).
[146] J. P. Hohimer, G. A. Vawter, and D. C. Craft, Appl. Phys. Lett. **62**, 1185–1187 (1993).
[147] T. Ben-Messaoud and J. Zyss, Appl. Phys. Lett. **86**, 241110 (2005).
[148] C. Li, N. Ma, and A. W. Poon, Opt. Lett. **29**, 471–473 (2004).
[149] D. J. W. Klunder, F. S. Tan, T. van der Veen, H. F. Bulthuis, G. Sengo, B. Docter, H. J. W. M. Hokstra, and A. Driessen, J. Lightwave Technol. **21**, 1099–1110 (2003).